

1 Revision 1: Sept. 30, 2020

2

3 Cr₂O₃ in Corundum: Ultra-high contents under reducing conditions

4

5 William L. Griffin^{1*}, Sarah E.M. Gain^{1,2}, Martin Saunders², Fernando Cámara³, Luca Bindi⁴, Deborah Spartà³, Vered
6 Toledo⁵ and Suzanne Y. O'Reilly¹

7

8 ¹ARC Centre of Excellence for Core to Crust Fluid Systems (CCFS) and GEMOC, Earth and Environmental Sciences,
9 Macquarie University, NSW 2109, Australia; bill.griffin@mq.edu.au

10 ² Centre for Microscopy, Characterisation and Analysis, The University of Western Australia, WA 6009, Australia

11 ³ Dipartimento di Scienze della Terra "Ardito Desio", Università degli Studi di Milano, Via Mangiagalli 34, I-20133
12 Milano, Italy

13 ⁴ Dipartimento di Scienze della Terra, Università di Firenze, Via La Pira 4, I-50121 Florence, Italy

14 ⁵Shefa Gems (A.T.M.) Ltd., Netanya 4210602, Israel

15

16 Abstract

17 Xenocrysts and xenoliths in Upper Cretaceous pyroclastics on Mount Carmel (N. Israel)
18 represent a series of similar magma-fluid systems at different stages of their evolution, recording a
19 continuous decrease in oxygen fugacity (fO_2) as crystallization proceeded.

20 Corundum coexisting with Fe-Mg-Cr-Al spinels, other Fe-Mg-Al-Na oxides and Fe-Ni alloys
21 in apparent cumulates crystallized at fO_2 near the iron-wüstite (IW) buffer ($fO_2 = IW \pm 1$) and is
22 zoned from high-Cr cores to lower-Cr rims, consistent with fractional crystallization trends. The
23 reconstructed parental melts of the cumulates are Al-Cr-Fe-Mg oxides with *ca* 2 wt% SiO₂.
24 Corundum in other possible cumulates that contain Cr-Fe (Fe 45 wt%) alloys has low-Cr cores and
25 still lower-Cr rims. Corundum coexisting with Cr⁰ ($fO_2 = IW - 5$) in some possible cumulates has low-
26 Cr cores, but high-Cr rims (to >30% Cr₂O₃). These changes in zoning patterns reflect the strong
27 decrease in the melting point of Cr₂O₃, relative to Al₂O₃, with decreasing fO_2 . EELS analyses show
28 that all Cr in corundum that coexists with Cr⁰ is present as Cr³⁺. This suggests that late in the
29 evolution of these reduced melts, Cr²⁺ has disproportionated via the reaction $3Cr^{2+}(\text{melt}) \rightarrow$
30 $2Cr^{3+}(\text{Crn}) + Cr^0$.

31 The most Cr-rich corundum crystallized together with β -alumina phases including
32 NaAl₁₁O₁₇ (diaoyudaoite) and KAl₁₁O₁₇ (kahlenbergite) and β'' -alumina phases; residual melts
33 crystallized a range of (K,Mg)₂(Al,Cr)₁₀O₁₇ phases with the kahlenbergite structure. The parental
34 melts of these assemblages appear to have been Al-Cr-K-Na-Mg oxides, which may be related to
35 the Al-Cr-Fe-Mg oxide melts mentioned above, through fractional crystallization or liquid
36 immiscibility.

37 These samples are less reduced (fO_2 from IW to IW-5) than the assemblages of the trapped
38 silicate melts in the more abundant xenoliths of corundum aggregates (fO_2 =IW -6 to -10). They
39 could be considered to represent an earlier stage in the fO_2 evolution of an "ideal" Mt Carmel
40 magmatic system, in which mafic or syenitic magmas were fluxed by mantle-derived CH_4+H_2 fluids.
41 This is a newly recognized step in the evolution of the Mt Carmel assemblages, and helps to
42 understand element partitioning under highly reducing conditions.

43

44 **Introduction**

45 Cr is a common multivalent element, and its oxidation state in minerals potentially carries
46 information on the oxygen fugacity (fO_2) of their crystallization environment (Schreiber and Haskin
47 1976). However, this feature is not generally useful in mantle petrology because the redox
48 reactions that define steps in the valence state of Cr occur at relatively low fO_2 compared to most
49 igneous and metamorphic environments, so that Cr^{3+} is the most common form. The $Cr^{3+}-Cr^{2+}$
50 transition (as defined by the $CrO-Cr_2O_3$ buffer reaction) lies at fO_2 just above the Iron- Wüstite
51 (IW) buffer (IW +0.5) (Fig. 1a), and is potentially observable in the most reduced parts of the deep
52 subcontinental lithospheric mantle (SCLM) (e.g. Yaxley et al. 2012). At high temperatures, the
53 reduction of Cr^{2+} to Cr^0 occurs at fO_2 of ca IW -5 (Fig. 1a), conditions that are not common on
54 Earth but must (as will be shown here) occur locally. To illustrate the behavior of Cr under highly
55 reducing conditions, we describe zoning patterns in a series of corundum cumulates, and report
56 the occurrence of corundum (ruby) with >30 wt% Cr_2O_3 and inclusions of Cr^0 and Cr_2N ; this
57 assemblage requires fO_2 near IW -5. We also attempt to define the petrological setting of this
58 assemblage within the evolution of a series of magmatic systems, some of which eventually
59 reached even more reduced conditions (Griffin et al. 2018a and references therein).

60

61 **Background**

62 The Cretaceous pyroclastic rocks of Mount Carmel (Northern Israel; Fig. SD-1) erupted
63 from 6-8 volcanic centres over the period 98-85 Ma, and over an area of at least 150 km².
64 Xenoliths and xenocrysts enclosed in these tuffs and in secondary alluvial deposits appear to
65 represent different aspects of similar magma-fluid systems at different stages of their evolution.
66 They record a wide range of oxidation states, including some of the most reducing conditions yet
67 reported in terrestrial rocks (Griffin et al. 2018a). As in other xenolith studies, a hypothetical
68 magma/fluid history has been constructed by piecing together information expressed in a suite of
69 xenoliths and xenocrysts. Specifically, it is possible to arrange the samples from Mt. Carmel in a

70 sequence of oxidation states (decreasing fO_2) that appears to record the evolution of magmas
71 fluxed by CH_4+H_2 at high fluid/rock ratios (Fig. 1b; Xiong et al. 2017; Griffin et al. 2018a, 2019a).
72 Grains of vesicular wüstite record fO_2 near the QFM buffer ($fO_2 = IW+3$ to $+4$). Large euhedral to
73 subhedral crystals of magnesian calcite have high-Sr cores with $^{87}Sr/^{86}Sr = 0.7033$, suggesting a
74 magmatic origin, and probably crystallized near the EMOD (enstatite-magnesite-olivine-diamond)
75 buffer (IW +1.5). Spheres of quenched Fe oxide-silicate and Ti oxide-silicate melts, many with
76 cores of native iron (Fe^0), suggest fO_2 near IW.

77 Among the most common xenoliths are aggregates of skeletal/hopper crystals of
78 corundum, which trapped pockets of Ca-Mg-Al-Si-O melts with high contents of Ti, Zr and REE.
79 Petrographic observations show that the earliest phenocrysts in these pockets are Mg-Al-Ti spinel,
80 followed by tistarite (Ti_2O_3) and then carmeltazite ($ZrAl_2Ti^{3+}_4O_{11}$; Griffin et al. 2018b). More
81 evolved melts precipitated REE-rich hibonite ($CaAl_{12}O_{19}$), moissanite (SiC) and Zr-REE phases. The
82 melt pockets also contain a variety of immiscible carbon-rich Fe-Ti-Zr silicide/phosphide melts,
83 which crystallized TiC, SiC, TiB_2 (Griffin et al. 2020a) and silicide phases. Crystals of moissanite (up
84 to 4 mm) contain inclusions of Si^0 melts that crystallized Fe-, Ca- and Al silicides (Huang et al.
85 2020). The crystallization of SiC and the reduction of Ti^{4+} to Ti^{3+} require $fO_2 = IW-6$ to $IW-7$ (Fig.
86 1a). The most evolved silicate melts produced coarse-grained hibonite+grossite+spinel aggregates
87 with inclusions of V^0 , requiring $fO_2 \leq IW-9$ (Griffin et al. 2019a). Even lower fO_2 may be implied by
88 the presence of Ti^{2+} -bearing phases such as TiB_2 (Griffin et al. 2020a). The most reduced conditions
89 imply a hydrogen-saturated environment, which has been confirmed by the discovery of VH_2
90 (Bindi et al. 2019) and the presence of abundant H_2 in the hibonite crystals that have inclusions of
91 V^0 (Griffin et al. 2020b).

92 Paragenetic studies (Xiong et al. 2017; Griffin et al. 2018a, 2019a) suggest that these
93 xenocrysts formed at ca 1 GPa, close to the crust-mantle boundary, and crystallized over a T range
94 of approximately 1450°C to 1200°C. Dating of large xenocrystic zircons from the pyroclastic rocks
95 (Griffin et al. 2018b) suggests that the crust was underplated by mafic magmas from ca 285-100
96 Ma and that these magmas differentiated to syenitic (*s.l.*) melts that crystallized large zircons and
97 typical basaltic sapphire, which also is found in the tuffs and alluvial deposits. We have previously
98 suggested that lenses of these syenitic (*s.l.*) residual melts in the underplate were reduced by
99 interaction with mantle-derived CH_4+H_2 fluids (Griffin et al. 2018a). The detailed evolution of
100 these melts will be discussed elsewhere; it appears to have involved multiple episodes of melt
101 immiscibility.

102 The range of fO_2 described above, as well as a common mineralogy and mineral chemistry,
103 suggests a common process linking the different occurrences. Most of the work so far has
104 concentrated on the highly reduced corundum aggregates (trademarked by Shefa Yamim as
105 Carmel Sapphire™) (Griffin et al. 2016; Xiong et al. 2017; Griffin et al. 2018a) and the still more
106 reduced hibonite-grossite- V^0 assemblage (Griffin et al. 2019a). Here we describe less-reduced
107 samples that illustrate the behaviour of Cr in one or more magmatic systems that were
108 crystallizing abundant corundum as fO_2 declined, ending with the appearance of native chromium
109 (Cr^0) at fO_2 near IW-5.

110

111 **Geological Setting and Provenance of Samples**

112 The material described here is derived from Cretaceous volcanic centers and related alluvial
113 (placer) deposits in the Mt Carmel-Yizre'el Valley area of northern Israel (Fig. 1). This area lies
114 within a complex system of minor rifts and other faults, related to the Africa-Arabia plate
115 boundary that later developed into the Dead Sea Transform, with >100km movement since the
116 initiation of offset in Miocene time. The NW-SE Carmel Fault that bounds Mount Carmel on the
117 east (Fig. 1) is part of the Carmel-Gilboa system, which forms a 10-20 km wide belt of faulting
118 running through the Yisre'el Valley, and may extend across the continental margin (Segev and
119 Rybakov, 2011). The SW side of Mount Carmel is dissected by multiple N-striking vertical faults
120 with offsets up to a few hundred meters. The basement rocks, which are not exposed in this area,
121 are considered to have formed in Pan-African (Cadomian) time (>620 Ma; Stein and Goldstein,
122 1996). The Galilee area represents a zone of thin continental crust, with a Moho depth of 23-32
123 km (Segev and Rybakov, 2011). The geophysical data, and estimates of the Cretaceous geotherm
124 from mantle-derived xenoliths and xenocrysts (Apter, 2014; our unpublished data) suggest a thin
125 (<100 km), hot lithospheric mantle. It is not clear whether this is a remnant of a previously thicker
126 lithosphere that was thinned during rifting and drifting, or has developed later through magmatic
127 processes (Stein and Hofmann, 1992).

128 The Late Cretaceous (98-94 Ma, Turonian-Cenomanian) volcanic activity of northern Israel
129 took place in the Mount Carmel-Umm El Fahm area (Fig. 1), and field relations have been
130 described in detail by Sass (1980). The dominant volcanic rocks are pyroclastics of mafic to
131 ultramafic composition; lava flows played a minor role in this volcanic activity. The volcanoes
132 erupted in a shallow marine environment, in intimate contact with carbonate sediments
133 containing rich assemblages of fossils. Several outcrops of black and variegated pyroclastics in
134 isolated areas west of Kerem Maharal (Fig. 2) overlie the Yagur Formation of Albian (Bein, 1974;

135 Rosenfeld and Raab, 1984) to earliest Cenomanian age (Lewy, 1991) and represent the first
136 volcanic eruptions in the area.

137 The eruptive vents are filled with quite fresh massive “black pyroclastics” (Fig. 2; Sass, 1980).
138 The more strongly layered “variegated pyroclastics” (Fig. 3) occur as packages of various thickness
139 locally interbedded with the carbonates, indicating pulsed explosive eruptions and the
140 construction and levelling of small seamounts (Sass, 1980). Some centers may be monogenetic,
141 but recent detailed examination of good outcrops in the Rakefet Magmatic Complex has identified
142 two, and possibly three, separate vents surrounded by the layered variegated pyroclastics. The
143 eruptions in the area took place mainly between 98 Ma and 95 Ma but continued up to *ca* 85 Ma.
144 Further details of the regional setting, stratigraphy, timing and sources of the volcanic rocks are
145 given by Griffin et al. (2018a). The uplift of Mt Carmel relative to the adjoining valleys and hills
146 began in Pliocene time and is continuing today.

147 The few basalt flows spatially associated with the Cretaceous volcanoes are porphyritic
148 alkali-olivine basalts with OIB-type trace-element signatures (Kaminchik et al., 2014) and their
149 relationship to the explosive magmatism is unclear (Sass, 1980). The ejecta from the explosive
150 volcanoes are dominated by “ash, which is made up of microvesicular glass in various degrees of
151 preservation [and] lapilli and volcanic bombs [of] vitrophyric basalt, rich in vesicles and consisting
152 of black glass (sideromelane), altered olivine phenocrysts and microlites of augite and plagioclase”
153 (Sass, 1980). The chemical composition of the parental magmas is difficult to define, because the
154 glassy lapilli typically show evidence of physical mixing between compositionally distinct melts
155 (SiO_2 53.5 vs 40.2 wt%), and complex textures of lapilli within lapilli. Furthermore, the glasses may
156 have been modified in the marine environment, as they typically contain very little Na or K. Lapilli
157 of microcrystalline basalts analysed by wide-area SEM-EDS ($n=50$) have a mean composition
158 corresponding to tholeiitic picrite or meimechite (SiO_2 43.5 %, MgO 14.8%; Griffin et al., 2016),
159 but low values of Na and K suggest that these compositions are also modified ().

160 The gem placers of the Kishon River are concentrated in the Mid-Reach zone (Fig. SD-1)
161 where the valley narrows to a gorge next to the escarpment along the northeast side of Mt
162 Carmel, and entrains coarser material coming down from Mt Carmel in alluvial fans. The
163 combination of increased flow rates and a larger coarse fraction has provided the conditions
164 necessary for development of transient placers in the confined channel. The placers sampled in
165 this work do not come from the current bed of the Kishon River; they are paleo-placers developed
166 at the base of Plio-Pleistocene terraces that now lie *ca* 10 meters above the current drainage. The
167 placers occur in unlithified and uncemented coarse gravels that directly overlie bedrock and are

168 overlain in turn by 4-10 meters of undisturbed finer-grained sediments. A typical section is shown
169 in Figure SD-2 together with an illustration of the types of material recovered from this 333-tonne
170 bulk sample.

171 During Shefa Yamim's exploration program, most of the known volcanic centers have been
172 sampled to determine their contents of potential gem minerals. The procedures for sampling and
173 processing, which are designed to exclude contamination with synthetic materials, are described
174 in the Appendix. This sampling has demonstrated that the volcanic centers, which lie at altitudes
175 50-350 meters above the Kishon river (Figure SD-1), collectively contain all of the minerals found
176 in the alluvial deposits, in particular moissanite and the type of ruby described in this paper (Table
177 SD-1; Fig. SD-3).

178 Most heavy-mineral concentrates from both the volcanic centers and the placer deposits are
179 dominated by the assemblage of low-chromium garnet, clinopyroxene (Cr-diopside), olivine, and
180 spinel, representing a mantle section of spinel peridotite with significant amounts of garnet±spinel
181 clinopyroxenite. These rock types are also found as small xenoliths in the pyroclastic rocks
182 (Mittlefeldt 1986; Kaminchik et al. 2014; references therein; authors' collections).

183 Some of the gem minerals, including ruby and moissanite, are present in the volcanic centers
184 at very low abundances even in samples of several tonnes, and only the Rakefet body has been
185 well bulk-sampled (>100 tonnes). Therefore the apparent absence of some minerals from some
186 bodies may simply reflect insufficient sampling. However, the results of the exploration campaign
187 confirm that the volcanic centers on Mt Carmel represent the primary sources of the gem material
188 in the alluvial placers.

189 Corundum and moissanite, along with the peridotite-pyroxenite suite of minerals, also are
190 common in surficial sediments and modern streams across the drainage basin of the Kishon River.
191 This distribution reflects a shallow Miocene marine incursion which resulted in locally-preserved
192 carbonate-cemented, quartz-rich beach placers rich in garnet, diopside, spinel and moissanite (Fig.
193 SD-4; Griffin et al., 2019b), which have been recycled back into the Pliocene and Pleistocene-
194 recent drainages. It therefore is difficult to evaluate the possible contribution of the Pliocene-
195 Pleistocene basalts in the Yizre'el Valeey to the gem placers (Fig. SD-1).

196

197

198 **Sample Descriptions and Analytical Methods**

199

200 Because the samples represent several types/stages, we discuss the mineral chemistry for
201 each group together with the petrographic descriptions. The mineral chemistry is presented in
202 Tables 1-4; analytical methods are given in the Appendix.

203
204 **1. Corundum cumulate/quench aggregate (1174-1A; Table 1)**

205
206 This is a single micro-xenolith 1.5 mm across (Fig. 5a,b), recovered from an alluvial bulk
207 sample in the Kishon Mid Reach Zone 1 (Fig. 2). One half consists mainly of elongate prisms of
208 corundum, and the subparallel alignment of the prisms suggests a cumulate texture. Large grains
209 are zoned in Cr₂O₃, with high-Cr cores (ca 15 wt% Cr₂O₃) separated by a diffuse boundary from
210 rims that are zoned from 8-10 wt% Cr₂O₃ near the cores to ca 6 wt% Cr₂O₃ in small irregular
211 overgrowths. The spaces between corundum prisms are mostly filled by Al-Mg-Fe-Cr spinel. Rare
212 grains of an Fe-Ni alloy with 1-2 wt% Cr occur in the rims of corundum prisms. The other half of
213 the grain has a pronounced barred structure (Fig. 6), with alternating lamellae of spinel and
214 corundum (8-9% Cr₂O₃) compositionally similar to the rims of the large grains in the coarser-
215 grained half. The barred structure is similar to that formed during eutectic crystallisation in some
216 synthetic systems.

217 The interstitial spinel in the coarse-grained portion, and that in the barred intergrowth, are
218 identical in composition. The structural formula (Table 1) suggests that ca 1/3 of the Fe (11-12
219 wt% as FeO) in the spinel is present as Fe³⁺, substituting for Al and/or Cr. In the barred
220 intergrowth, the spinel and corundum are crosscut by, and intergrown with, abundant laths of an
221 unknown Na-rich phase ((Na,Fe,Mg)₂(Al,Ti,Cr)₆O₁₁) with a large deficit in the analytical sum, fewer
222 dark laths of composition (Fe,Mg)(Al,Cr,Ti,Si)₈O₁₃, also with a deficit, and small grains of an Fe-Cr-
223 Al spinel ((Fe,Mg,Ni)(Al,Cr)₂O₄). Irregular patches of a phase with the composition of K-free
224 nepheline (NaAlSiO₄) occur interstitially between spinel and corundum. The Raman spectrum of
225 this phase (Figure SD1) does not correspond to that of the synthetic phase known as "carnegieite"
226 (Bowen 1912) and reported by Richet and Mysen (1999). Tiny grains of an unknown Zr oxide
227 (Zr₂O₃) are common, as are rare grains of an Fe-Ni-Cr alloy and an Fe-Cr alloy.

228 SEM-EDS areal analyses (in which an integrated spectrum is acquired in scanning mode)
229 were done for the central portions of both the barred area and the coarse-grained area, as well as
230 the whole grain (Fig. 5a; Table 1). The coarse-grained area is higher in Al₂O₃ and Cr₂O₃ than the
231 barred area, but the latter is higher in SiO₂, TiO₂, FeO, MgO and Na₂O. This would be consistent
232 with a cumulate-residual melt relationship between the two parts of the grain, as suggested by
233 the petrography. Ni is below detection in the EDS areal analyses; it is concentrated in the rare Fe-

234 Ni alloy grains and the Fe-Cr-Al spinel. Na is distributed between nepheline and the
235 $(\text{Na,Fe,Mg})_2(\text{Al,Ti,Cr})_6\text{O}_{11}$ phase, while Zr is concentrated in the Zr_2O_3 grains.

236
237 **2. Corundum "cumulates" with metal alloys (1210B-4, 5; 1125-2D; Table 2)**
238

239 Samples 1210B-4 and -5 were recovered from one alluvial bulk sample in the Kishon Mid
240 Reach Zone 1, and 1125-2D from another (Fig. 2). In the first two, the corundum crystals are
241 blocky and euhedral against a matrix of a K-Al oxide (Fig. 7a,b). The corundum crystals appear to
242 be touching, suggesting a cumulate texture. 1210B-4 (Fig. 7a) contains scattered balls of a Cr-Fe-
243 Ga alloy, mainly in outer parts of corundum grains or in the matrix. 1210B-5 (Fig. 7b) contains
244 abundant spheres of Cr metal (Cr^0) with ca 0.1 wt% Si, but no Fe or Ga; smaller spheres occur in
245 corundum cores, and larger ones in the rims. The spherical form of the metallic grains strongly
246 suggests an origin as immiscible melts.

247 Sample 1125-2D (Fig. 7c) has a different structure; similarly-sized laths of corundum and a
248 K-Al oxide are jumbled together, with no obvious foliation; this is especially apparent when
249 comparing the element-distribution maps for Al and K (Fig. 7c). The corundum cores contain 4-5
250 wt% Cr_2O_3 , and each has a well-defined rim with a mean 27 wt% Cr_2O_3 , grading rapidly to
251 outermost rims with ca 34 wt% Cr_2O_3 . Numerous spheres of Cr^0 occur in the corundum rims, and
252 many smaller ones at their contacts with the K-Al oxides; larger spheres in the corundum rims are
253 surrounded by narrow zones depleted in Cr. There are also numerous angular voids between
254 crystals of the K-Al oxide.

255 The corundum grains in 1210B-4 are zoned from 2.5 wt% Cr_2O_3 in the cores, to a mean of
256 1.3 wt% in the rims, but there are local overgrowths containing up to 5 wt% Cr_2O_3 . The corundum
257 in 1210B-5 is mostly low in Cr; cores of grains contain 0.2 % Cr_2O_3 , and most rims 0.4%, but locally
258 rims contain up to 2.4 wt% Cr_2O_3 . In both cases Cr is concentrated in the metallic melts, but these
259 melts appear to have separated from the oxide melt before corundum crystallized in 1210B-5 and
260 later in 1210B-4 and 1125-2D. It is notable that these samples contain no Fe other than that in the
261 alloy grains in 1210-B4. The matrix ranges in composition from $\text{Na}(\text{Al,Cr})_{11}\text{O}_{17}$ (diaoyudaoite; Shen
262 et al. 1986) in 1210B-4 to $\text{KAl}_{11}\text{O}_{17}$ (kahlenbergite; Krüger et al. 2019) in 1210B-5 and 1125-2D.
263 Raman spectroscopy (Fig. SD2) confirms the identification of the K-Al oxide in 1210B-5 as
264 kahlenbergite.

265
266 **3. Large hopper crystals of Cr-rich ruby (1174-C; 1175-A; Table 3)**
267

268 These two samples were recovered from separate alluvial bulk samples in the Kishon Mid
269 Reach Zone 1 (Fig. 2). Sample 1174-C is a 1.7-mm grain with a hollow center and raised rims,
270 indicating hopper growth, and it has an intense purple-red colour (Fig. 8a). The surface of the
271 crystal (Fig. 8b, c) is decorated with balls of Cr⁰ up to 60 microns across, and very small grains of an
272 Fe-Ni alloy. It is strongly zoned in Cr from central parts with 1-4% Cr₂O₃, rising to mean values of
273 ca 23 wt% Cr₂O₃ toward both the outer rim and the edge of the central cavity. Single EMP spots in
274 these zones contain up to 33% Cr₂O₃, and corundum adjacent to the Cr⁰ balls has mean values >31
275 wt% Cr₂O₃. The most Cr-rich portions of the crystal are finely granular in BSE imagery, suggesting
276 an intergrowth of higher- and lower-Cr corundum on the scale of a few microns (Figs 8a,c). TEM
277 images (Fig. 8d) of these zones show an intergrowth of micrograins with ca 30% (Cr# = 0.22) and
278 ca 58% Cr₂O₃ (Cr# = 0.48) respectively. The Cr⁰ sphere shown in the FIB foil is separated from the
279 Cr-rich corundum by a 5-µm zone of a chromium nitride. In other areas the Cr⁰ spheres are
280 separated from the corundum by a Mg-Cr-Al spinel.

281 LA-ICPMS analysis (Table 3) shows that the high-Cr areas of grain 1174-C also have more
282 Mg, P, Ti, V, Ga and Zr than the low-Cr portions. However, Ga levels are extremely low in both
283 types, compared to most natural corundum (cf Sutherland et al., 2014). A K-Al-oxide phase with
284 low contents of Cr and a composition corresponding to kahlenbergite occurs as a patchy outer rim
285 and within the central cavity (Fig. 5b,c). EMP analysis and TEM-EDS show that the largest Cr⁰ ball
286 is essentially pure Cr (Fig. 5c) with traces of Si, Al and Mn. EELS analysis (Fig. 9) shows that Cr in
287 both the low-Cr and high-Cr parts of the corundum occurs as Cr³⁺.

288 The Cr-nitride phase has the composition Cr_{1.8}N, based on TEM-EDS analysis. EELS analysis
289 (Fig. 9; cf. Daulton and Little 2006) suggests that Cr in the nitride phase has a valence ≤2. Electron
290 diffraction images indicate that the crystal structure of the nitride is similar to that of synthetic
291 Cr₂N (*P*-31m, ordered structure). A natural phase with the composition Cr₂N has been reported
292 previously by Harries and Langenhors (2011) in the chondritic meteorite CM2 Y-793321.

293 Sample 1175A was a 2-mm hopper crystal prior to polishing, and shows irregular zoning in
294 Cr, some related to internal crystal faces (Fig. 10). The original parts of the grain (dark in BSE
295 images) contain <1% Cr₂O₃, while tendrils of higher-Cr corundum extend outward from a euhedral
296 crystal of a K-Al oxide (KAl₁₁O₁₇; probably also kahlenbergite) near the middle of the crystal. These
297 tendrils (lighter in BSE images) range from 7.7 - 10.6 wt% Cr₂O₃, with the highest-Cr corundum
298 concentrated around the central K-Al-oxide. The higher-Cr zones include several small grains of an
299 Mg-Al-Cr spinel and one of a Mg-Cr spinel. A single large metallic inclusion (Fig. 10) is divided
300 60:40 between Cr⁰ and a nitride phase. SEM-EDS analysis gives the approximate composition

301 $\text{Cr}_{1.3}\text{N}$, but N is likely to be underestimated relative to the windowless EDS technique used in the
302 TEM-EDS analyses (cf. Table 3).

303 304 **4. Irregularly zoned ruby grains with alloy inclusions (1210A-1,2; 1210B1-3; Table 4)**

305
306 These five xenocrysts are similar in colour to those described in section (3) above, and
307 show irregular zoning visible in BSE images and maps of Cr distribution. In samples 1210A-1,2 and
308 1210B-1 (Fig. 11a, b), mm-scale prisms of low-Cr corundum are roughly aligned, suggesting a
309 cumulate texture. The laths are irregularly overgrown and partially replaced by zoned rims of
310 higher-Cr corundum, associated with abundant spheres and elongated amoeboid grains of Cr
311 metal (Cr^0). In some cases the metal grains are aligned along the contact between the core and
312 rim. Others are interstitial to low-Cr laths that show no overgrowth by Cr-rich corundum. Some
313 grains contain interstitial void spaces. Small interstitial patches of the K-Al-oxide phases seen in
314 other samples are present in the grains shown in Figure 11, and some contain rare grains of spinel
315 with inclusions of Cr^0 . Sample 1210-B1 (Table 4; Fig. 11b) contains spheres of a Cr-Fe-Ga alloy
316 similar to that in 1210B-4 (Table 2), many aligned along a single crystal face.

317 Sample 1210B-3 (Fig. 11c) is a skeletal crystal, consisting mainly of low-Cr corundum (<1
318 wt% Cr_2O_3), with the internal channels filled with a K-Mg-Al-oxide phase ($(\text{K},\text{Mg})_{2.12}\text{Al}_{10.62}\text{O}_{17}$;
319 probably β'' -alumina). The Cr_2O_3 content of the corundum rises to >7 wt% in the rims adjacent to
320 these channels.

321 The dark-BSE cores of these grains typically contain <3 wt% Cr_2O_3 . The inner parts of light-
322 BSE zones, and rims without further overgrowths, have 8-20 wt% Cr_2O_3 while the outer parts near
323 the metallic inclusions may contain 35-40% Cr_2O_3 . The metallic spheres are Cr^0 with 0.2-0.9 wt%
324 Si. The highest Si values tend to be found in spheres sited between the cores and rims of the
325 corundum laths, while lower values occur in Cr^0 balls in the highest-Cr outer rims of the corundum.
326 One analysis of a spinel shows 35 wt% Cr_2O_3 ; the structural formula indicates that ca 16% of the Cr
327 substitutes in the Mg site, suggesting the presence of both Cr^{2+} and Cr^{3+} . The composition of the
328 β -alumina phase varies from grain to grain. The Mg,Cr-rich variety ranges from
329 $(\text{K},\text{Mg})_{1.21}(\text{Al},\text{Cr})_{10.93}\text{O}_{17}$ to $(\text{K},\text{Mg})_{2.13}(\text{Al},\text{Cr})_{10.63}\text{O}_{17}$, and the K-rich one from $\text{K}_{1.36}(\text{Al},\text{Cr})_{10.88}\text{O}_{17}$ to
330 $\text{K}_{1.09}\text{Al}_{10.97}\text{O}_{31}$.

331

332 **Discussion**

333 This discussion is based on the working hypothesis outlined above, that the Mt Carmel
334 xenoliths represent snapshots of similar melt-fluid systems, captured at different stages of their
335 evolution by ascending magmas over a period of *ca* 15 million years.

336 1. *Cr-nitrides*

337 The Cr-nitride phases present in samples 1174C and 1175A (Table 3; Figs 8 and 11) are
338 significant in understanding the evolution of the system. In the phase diagram for the Cr-N binary
339 (Fig. 12) $\text{Cr}_{2+x}\text{N}_{1-x}$ crystallizes together with Cr^0 at a eutectic point (*ca* 1640 °C), and approaches the
340 Cr_2N stoichiometry on cooling to below 500°C. At higher N/Cr, Cr_2N crystallizes together with
341 nearly stoichiometric CrN at another eutectic near 1640 °C, and thus CrN should not be in
342 equilibrium with Cr^0 . It is likely that the presence of abundant C and H in the system would
343 significantly lower the liquidus temperatures of the metallic melts (Griffin et al. 2020b).

344 The EELS spectra of the $\text{Cr}_{1.8}\text{N}$ phase in sample 1174C (Fig. 9) are most consistent with a
345 valence ≤ 2 (Dalton and Little 2006). In Cr_2N the nominal valence of Cr would be $\text{Cr}^{1.5+}$, but Cr_2N is
346 an interstitial compound, in which the N atoms occupy octahedral holes among the Cr atoms, and
347 neither element actually exists as ions. Several experimental studies suggest that the Cr_2N
348 observed in sample 1174C could be the product of a subsolidus reaction, rather than
349 crystallisation from a melt. For example, Lyutaya and Kulik (1974) demonstrated that the reaction
350 of N with Cr can result in the simultaneous formation of Cr_2N and CrN, but that Cr_2N is more
351 stable. In experiments with the oxidation of Cr-N alloys (Krzanowski and Foley 2014), a layer of
352 Cr_2N typically formed between the Cr and the surficial oxide (Cr_2O_3 , analogous to the high-Cr
353 corundum in sample 1174C (Fig. 8d)). We therefore suggest that the Cr_2N in this example formed
354 through the exsolution of N from the crystallizing droplets of Cr melt on the surface of the
355 corundum crystal, and the back-reaction of N with the solidified Cr^0 .

356

357 2. *β -alumina, β'' -alumina and K-Na-Mg-alumina phases*

358 The alumina phases coexisting with Cr-rich corundum $\pm \text{Cr}^0$ fall into four groups. One
359 (sample 1210B-4, Table 2) is Na-rich, with the formula $(\text{Na}_{0.99}\text{K}_{0.03}\text{Ca}_{0.02})_{\Sigma 1.03}(\text{Al}_{10.58}\text{Cr}_{0.35}\text{Mg}_{0.05})_{\Sigma}$
360 $_{11.01}\text{O}_{17}$; this corresponds to the synthetic phase Na- β -alumina ($\text{NaAl}_{11}\text{O}_{17}$) (Beevers and Ross 1937)
361 and the mineral diaoyudaoite (Shen et al. 1986). The analogous K- β -alumina phase is observed in
362 *inter alia* sample 1210B-1 (Table 4), with the composition
363 $(\text{K}_{0.95}\text{Na}_{0.01}\text{Ca}_{0.01})_{\Sigma 0.97}(\text{Al}_{10.70}\text{Mg}_{0.22}\text{Cr}_{0.16})_{\Sigma 11.08}\text{O}_{17}$. These two phases are typically found as the cores
364 of lath-shaped grains. In a third population, which includes some overgrowths on K-rich laths, the
365 ratio $(\text{Al}+\text{Cr})/(\text{K}+\text{Na}+\text{Mg})$ (atomic %) has a narrow range of lower values (5.9-6.4) and slightly

366 higher Mg, corresponding to a formula of $K_{1.4}(Al,Cr)_{9.5}O_{17}$. This is similar to the formula for the
367 synthetic phase β'' -alumina, $K_{1.6}Al_{10.7}O_{17}$, and in the binary liquidus plot of the $K_2O-Al_2O_3$ system
368 (Fig. 13; Kim et al. 2018) the analytical points cluster around the molar composition of β'' -alumina.
369 Synthetic β'' -alumina is commonly stabilized by the addition of Mg, and like the β form, can have
370 widely variable stoichiometry. A wide range of divalent and even trivalent β'' -alumina phases has
371 been synthesised; most are stable over only a narrow T range (Farrington and Dunn 1982;
372 Schaeffer et al. 1990).

373 A fragment of the K- β -alumina phase from sample 1210B-1 (Table 4) was separated and
374 analysed by single-crystal XRD. It proved to be almost pure kahlenbergite, hexagonal $P6_3/mmc$,
375 with $a = 5.59765(10)$ Å, $c = 22.7141(4)$ Å, $V = 616.366(18)$ Å³, $Z = 2$. A complete data collection of
376 diffraction intensities was performed, and the structure was solved and refined (CIF file deposited
377 as supplementary material). A fragment of the diaoyudaoite from sample 1210B-4 (Table 4) has
378 the hexagonal space group $P6_3/mmc$, cell parameters $a = 5.60170(10)$ Å and $c = 22.6604(4)$ Å, $V =$
379 $615.797(19)$ Å³, $Z = 2$. A complete data collection of diffraction intensities was performed, and the
380 structure was solved and refined (CIF file deposited as supplementary material). These are
381 comparable to $a = 5.64860(6)$ and $c = 22.8970(3)$ for the type material from the Hatrurim basin
382 (Israel; Krüger 2019; Krüger et al. 2019), corresponding to synthetic K- β -alumina (Dernier and
383 Remeika 1976), and $a = 5.602(1)$ Å and $c = 22.626(5)$ Å for diaoyudaoite (Shen et al. 1986), also
384 corresponding to synthetic Na- β -alumina (Edström et al. 1991).

385 The type material of kahlenbergite occurs in pyrometamorphic hornfelses,
386 metamorphosed at ca 1200 °C. It contains 17% Fe_2O_3 , while the phase analyzed in our samples
387 contains no Fe, but minor amounts of Na, Mg and Cr; these chemical differences probably account
388 for the small differences in unit-cell values between our material and the type specimen.
389 Diaoyudaoite has been found in the heavy-mineral (S.G. > 2.8) fraction that makes up about 1.4
390 wt% of the surface layer of sea-floor muds at a depth of about 1500 m near the island of
391 Diaoyudao, a few kilometers northeast of Taiwan. Diaoyudaoite from the type locality contains
392 inclusions of Cr^0 , indicating a strongly reduced environment like the one described in this work.

393 The fourth type of alumina has much higher Mg contents, generally higher Cr and lower Na
394 contents, and $(Al+Cr)/(K+Na+Mg)$ of 2.6-4.7 (mean 3.2), corresponding to a formula of
395 $(K_{0.51}Mg_{0.46}Na_{0.03})_{2.12}(Al_{0.94}Cr_{0.06})_{9.78}O_{17}$. The examples analysed here contain 15-20 mol% MgO
396 (mean molar $MgO/K_2O = 1.9$) and 4.2 mol% Cr_2O_3 .

397 The most reliable available experimental and theoretical data on the $K_2O-MgO-Al_2O_3$
398 system are summarized by Kim et al. (2018). In the $K_2O-Al_2O_3$ binary (Fig. 13), the β phase

399 crystallizes via the peritectic reaction $\text{Crn} + \text{Liq} \rightarrow \beta\text{-alumina}$, while the β'' phase appears at
400 subsolidus temperatures as a result of reaction between β -alumina and KAlO_2 . The petrographic
401 relationships between corundum, the β -alumina phases and the K,Mg-alumina phase suggest that
402 the β -alumina (both Na- and K- variants) represents primary igneous phases, crystallizing together
403 with the corundum to produce cumulate-like textures, while the K,Mg-alumina phase represents
404 interstitial melts and/or products of reaction between residual melts and the cumulate phases.
405 This is consistent with the $\text{K}_2\text{O-MgO-Al}_2\text{O}_3$ liquidus diagram (Fig. 14), in which the K,Mg-alumina
406 phases plot along the β -alumina + spinel + liq cotectic, consistent with them representing MgO-
407 rich liquids in equilibrium with solid β -alumina phases. The reaction point $\beta + \text{Al}_2\text{O}_3 + \text{spinel} + \text{melt}$ at
408 1932°C corresponds to the assemblages observed in samples 1174 and 1175A (Table 3). The
409 range of intermediate compositions may reflect analysis of fine-grained mixtures of these
410 components.

411 We are not aware of any data pertaining to the effect of pressure on the phase diagram in
412 this system. However, crystallization temperatures may have been significantly lowered (to 1400-
413 1500°C ; Griffin et al. 2018a, 2019a) by the reduced volatile components required to produce the
414 very low $f\text{O}_2$.

415

416 3. Oxygen fugacity of different assemblages; behaviour of Fe, Ni, Ga and Cr

417 These samples cover a significant range of $f\text{O}_2$; their common feature is the presence of Cr-
418 rich corundum. Sample 1174-1A (section (1) above) differs from the others in that several of the
419 analysed phases contain small amounts of Fe, especially concentrated in the spinel, in which *ca*
420 $1/3$ of the Fe is present as Fe^{3+} . The distribution of $\text{Al}/(\text{Al} + \text{Cr})$ between spinel and corundum in
421 sample 1174-1A (Table 1) is consistent with equilibrium at *ca* 1200°C and $f\text{O}_2 = \text{IW to IW}+4$ (Jung et
422 al. 2005; Fig. 1). This distinguishes the sample from the more strongly reduced assemblages
423 observed in the melt pockets of the Carmel Sapphire aggregates from Mt Carmel, in which Fe is
424 found only in alloy phases and Fe-Ti silicides, with estimated $f\text{O}_2 = \text{IW}-6$ to -7 (Griffin et al. 2016,
425 2018a). We suggest that the assemblage in sample 1174A-1 probably crystallized at $f\text{O}_2$ somewhat
426 higher than IW, where Fe alloys could coexist with $\text{FeO-Fe}_2\text{O}_3$ bearing phases like spinel. The
427 spinel in sample 1175A, in contrast, contains no Fe, and the structural formula
428 $((\text{Mg}_{0.85}\text{Cr}_{0.15})(\text{Cr}_{0.43}\text{Al}_{1.57})\text{O}_4)$ suggests that some of the Cr is divalent, consistent with the
429 coexistence of this spinel with Cr^0 .

430 The behaviour of Fe and Ni in these samples is consistent with a progressive lowering of $f\text{O}_2$.
431 These elements are concentrated in both oxide phases and minor Fe-Ni alloys in Sample 1174-1A,

432 and the minor amounts of Fe in the corundum (Table 1) may be present as Fe³⁺. Small grains of
433 Fe-Ni alloys occur on the surface of grain 1174C (Fig. 8b), but no Fe is present in either the
434 corundum or the Cr⁰ on its surface. In samples 1210B-4 (Table 2) and 1210B-1 (Table 4) Fe occurs
435 only as a minor component in Cr-Fe-Ga alloys; in the remainder of the samples the Cr alloys
436 contain trace amounts of Si, but no Fe, Ni or Ga. This suggests that by the point that fO_2 had
437 dropped to near that of the CrO-Cr⁰ buffer, most Fe, Ni and Ga had been removed from the
438 system. It is notable that the Ga contents of the corundum varieties described here (< 0.3 ppm;
439 Table 3) are dramatically lower than those of other mantle-derived corundum (typically 50-150
440 ppm Ga₂O₃; Giuliani et al. 2015; Sutherland et al. 2009). This depletion may reflect the
441 sequestration of Ga in the metallic alloys at $fO_2 \leq IW$.

442 The Electron Energy Loss Spectroscopy (EELS) analyses (Fig. 9) of sample 1174C (section 3,
443 above) indicate that the oxidation state of the Cr varies from Cr³⁺ in the corundum (both low-Cr
444 and high-Cr types) to Cr²⁺ (or possibly Cr¹⁺) in the Cr-nitride and to Cr⁰ in the chromium metal. As
445 discussed above, Cr₂N crystallizes together with Cr⁰ (containing 3-4 wt% N) at a eutectic at 1640
446 °C, at 1 atm. These temperatures are almost certainly maximum values, with the real
447 temperatures being lowered by the presence of abundant volatiles (CH₄, H₂; Griffin et al. 2019a,
448 2020b; Bindi et al. 2019) in the Mt Carmel system. Pressure effects (from 1 atm to ca 1 GPa) are
449 difficult to quantify, but the melting points of alloys and metals typically increase only by ≤100
450 °C/GPa (e.g. Sinmyo et al., 2019).

451 The fO_2 of the CrO-Cr⁰ buffer (Fig. 1a) lies at ca IW-5, less reducing than the conditions
452 inferred from the Ti³⁺-bearing, but Cr-free, assemblages in the Carmel Sapphire, but more
453 reducing than in the Fe³⁺-bearing sample 1174A-1. Following the working hypothesis outlined
454 above, the high-Cr rubies described here thus appear to represent an intermediate stage in the
455 crystallization of the Mt Carmel magmas, preceding the onset of immiscibility between silicate
456 melts and Fe-Ti-silicide melts, and the crystallization of the Carmel Sapphire aggregates..

457 458 4. Evolution of the Crn-Esk system 459

460 The corundum-eskolaite (Al₂O₃-Cr₂O₃) system at 1 atm in air (Fig. 15) is described by a
461 continuous solid-solution loop, such that a melt with a given Cr# will precipitate a Cr-Al oxide with
462 higher Cr#, and fractional crystallization with decreasing T will precipitate corundum with
463 progressively lower Cr#. The subsolidus system contains a solvus and a spinodal, with critical
464 temperature at 945 °C (Fig. 15), and limited data suggest that these are not pressure-sensitive
465 (Degterov and Pelton 1996). The two populations of Cr-rich corundum identified in the TEM study

466 of sample 1174c (Table 2) do not define an isothermal pair on the solvus curve or the spinodal;
467 their separation could suggest that the crystal may have cooled to these temperatures prior to
468 eruption and quenching, but the solvus may also be shifted, relative to the experimental system,
469 by the presence of minor elements.

470 While the melting point of Al_2O_3 does not vary with $f\text{O}_2$, the melting point of Cr_2O_3 is
471 strongly $f\text{O}_2$ -dependent (Fig. 16; Degterov and Pelton 1996; Jung et al., 2005). At $f\text{O}_2 \geq \text{IW}$, the
472 melting point of the Cr_2O_3 end member is ca 300 °C higher than that of Al_2O_3 , and fractional
473 crystallization of corundum will produce “normal” zoning in which rims of grains will be less Cr-rich
474 than the cores. At $f\text{O}_2 = \text{ca IW} - 1$, the Al_2O_3 and Cr_2O_3 end members have similar melting points,
475 and the solidus and liquidus converge to a minimum close to the Al_2O_3 side. At the CrO-Cr⁰ buffer
476 ($f\text{O}_2 = \text{IW} - 5$) the melting point of the Cr oxide is ca 200°C below that of Al_2O_3 (Fig. 16d), and
477 fractional crystallization of low-Cr# corundum will drive the melt, and the later-crystallizing
478 corundum, toward higher Cr# (“reverse” zoning).

479 This behaviour offers an experimental explanation for the types of zoning displayed by the
480 samples described here. The large high-Cr corundum cores in sample 1174A-1 (Table 1) have Cr#
481 = 0.11, consistent with crystallisation from the reconstructed melt with Cr# = 0.07 at $f\text{O}_2 > \text{IW} + 1$,
482 when the solid-solution liquidus-solidus loop is still tilted downward from Cr to Al (Fig. 13a).
483 However, the Cr# of the reconstructed melt is effectively identical with the Cr# of the rims on the
484 large corundum prisms, and the corundum in the barred intergrowths. This situation is consistent
485 with a drop in $f\text{O}_2$ from $\geq \text{IW} + 1$ to ca IW - 1 during the crystallisation of the residual melt, such that
486 the solid-solution loop becomes nearly horizontal (Fig. 13b).

487 Most of the other grains described here (Tables 2, 4) have cores with low Cr#, zoned to
488 rims with higher Cr#. The core-rim differences in Cr# among these grains range from 0.04 to 0.20.
489 This is the predicted trend of fractional crystallisation at $f\text{O}_2 \ll \text{IW}$, as the slopes of both the
490 solidus curve and the liquidus curve become more steeply negative with falling $f\text{O}_2$, and the gap
491 between them widens (Fig. 16d). At such low $f\text{O}_2$, continued fractional crystallization of low-Cr
492 corundum will drive the melt, and the crystallizing corundum, toward higher Cr#, and eventually
493 to the separation of immiscible Cr-rich metallic melts.

494 Core-rim tie lines plotted on Figures 16c,d show that in most cases the rims are more Cr-
495 rich than the melt that would coexist with the cores, and overgrowths on the rims, where present,
496 are even more Cr-rich. If crystallization occurred in closed systems, these compositions suggest
497 that the melts continued to evolve to higher Cr# as temperature declined by ca 100-150 °C. As
498 noted above, the real temperatures would be significantly below those in the experimental

499 system, in the presence of fluids dominated by CH_4+H_2 . For example, a hydrogen pressure of 1
500 GPa would lower the melting point of Cr^0 by *ca* 700 °C (to *ca* 1350 °C) relative to the H-free
501 system (Fukai, 1992). A corundum-dominated fractional-crystallization process linking cores and
502 rims is also consistent with the increase in Mg, P, Ti, V and Zr from low-Cr cores to high-Cr rims in
503 sample 1174C (Table 3).

504 However, some of the highest Cr contents in the corundum may reflect another process.
505 In sample 1174C (Table 3, Fig. 8) the coexistence of Cr in at least three oxidation states (Cr^0 , Cr^{1+} ?,
506 Cr^{2+} , Cr^{3+}) suggests that the highest mean Cr contents of the corundum (33-40% Cr_2O_3) may reflect
507 the reaction 3Cr^{2+} (in melt) $\rightarrow 2\text{Cr}^{3+}$ (in corundum) + Cr^0 . As noted above, some Cr^0 spheres in
508 corundum appear to have narrow “haloes” depleted in Cr relative to the corundum a few microns
509 away (see Fig. 11a). This feature suggests that once they were trapped, the metallic balls
510 continued to grow by extracting Cr^{3+} from the corundum; this could imply even further reduction
511 during cooling.

512

513 5. *Origin of the parental melts*

514 Two different types of Al-rich oxide melts are represented by the samples described here,
515 one enriched in Fe, Ti, Zr and Cr (Table 1), and the other enriched in Cr, Na and K; their common
516 link is their Cr content. This dichotomy suggests the development of liquid immiscibility during the
517 evolution of an original parental oxide melt. Small-scale separation into silica-poor mafic melts
518 enriched in HFSE and transition elements, *versus* silica-alumina-rich melts that concentrate alkali
519 elements, has been noted in basaltic systems worldwide, but oxide melts generated through liquid
520 immiscibility are rarely erupted due to their high density (e.g. Philpotts and Doyle 1983; Charlier et
521 al. 2011; Kamenetsky et al. 2013).

522 In the aggregates of Carmel Sapphire that crystallized at lower $f\text{O}_2$ than the Cr-rich
523 assemblages, melt immiscibility is texturally evident in the apparent coexistence of Fe-Ti-Si-C
524 melts, the Si-rich but oxygen-poor melts that crystallized most Mt Carmel SiC (Huang et al., 2020),
525 and the residual Ca-Al-Mg silicate melts from which the Carmel Sapphire crystallized (Griffin et al.,
526 2016, 2018, in prep.).

527 The skeletal/hopper morphology of the Carmel Sapphire aggregates (Griffin et al., 2016)
528 reflects rapid growth from a magma supersaturated in Al_2O_3 , and this apparently coincided with
529 desilication of the silicate melt via the separation of Fe-Ti-silicide melts. Modelling of the growth
530 patterns preserved in the zoning of Ti^{3+} in the individual crystals (Bravo et al., 2020) suggests that
531 the Carmel Sapphire aggregates formed in very short-lived (days to years) channels filled with

532 flowing melts, immediately prior to eruption of the host magma. In contrast, the cumulate nature
533 of the Cr-rich samples described here suggests a process occurring in a more stable environment,
534 such as small magma chambers or mush pools.

535 The megacrystic sapphire and zircon found in the Mt Carmel tuffs are also well-known as
536 xenocrysts in alkali basalts worldwide. They are generally ascribed to crystallization from syenitic
537 (s.l.) differentiates of deep-seated basalts (Sutherland et al., 2009, references therein), which
538 would be consistent with other evidence for a thick basaltic underplate near the crust-mantle
539 boundary beneath Mt Carmel (Griffin et al., 2018c). Melt immiscibility in such systems, already
540 saturated in Al_2O_3 to the extent of crystallizing large corundum crystals, could be a starting point
541 for the development of oxide melts of the type represented by sample 1174A of this paper (Table
542 1). The conjugate silicate melts may be represented among the silicate-glass rims found on many
543 xenocrysts. Many details of such an evolution remain to be clarified, and will be reported
544 elsewhere.

545

546 6. Comparison with other Cr-rich corundum

547

548 The rubies described here include many that are more Cr-rich than any previously known
549 examples. Cr-rich rubies in serpentinites and eclogites can contain up to 13 wt% Cr_2O_3 (Grapes
550 and Palmer 1996; Janak et al. 2015). For mantle-derived samples, high-Cr rubies found as
551 inclusions in diamonds from the Juína kimberlite and the related Sao Luis alluvial deposits in Brazil
552 have held the previous records; Hall et al. (1994) reported an inclusion with 8.6 wt% Cr_2O_3 , and
553 Hutchinson et al. (2004) reported one with 13.4 wt% Cr_2O_3 . These are similar to the compositions
554 observed in sample 1174-1A (Table 1, Fig.2), but much lower in Cr than the rubies that coexist with
555 Cr^0 . The latter also are much more Cr-rich than synthetic rubies made by reaction of chromite
556 with Al^0 to give Cr-corundum + Cr^0 , and differ from such synthetic rubies in having much lower
557 contents of Mg, Fe, Mn, Ni, Ti, Ga, Sr and Ca (Hutchinson et al. 2004).

558 The corundum-bearing diamonds from Juína are Type II stones, which recently have been
559 shown to be derived from sublithospheric depths (Smith et al. 2016). Hall et al. (1994) suggested
560 that the high Cr_2O_3 content of their Juína inclusion could reflect a pressure effect. However,
561 studies of inclusions in a range of Type II diamonds have shown that these diamonds probably
562 grew in pools of molten Fe (Smith et al. 2018), which is consistent with the presence of ca 1% FeO
563 in the corundum inclusions. Under these conditions any COH fluid will be dominated by CH_4+H_2 ,
564 as shown by the gas inclusions observed in Type II diamonds (Smith et al. 2016). In an ultramafic
565 mantle, the presence of molten Fe would constrain $f\text{O}_2$ to near the IW buffer, where Cr would

566 exist mainly as Cr^{3+} or Cr^{2+} , and thus would concentrate in other melts/fluids rather than in the
567 molten Fe. The Cr-rich corundum inclusions in the Juína diamonds, and those in sample 1174-1A,
568 thus may approximate the maximum possible Cr_2O_3 content in corundum at $f\text{O}_2 = \text{IW}$.

569 570 **Summary**

571 The Cr content of corundum crystallizing from Al-rich melts beneath Mt Carmel in
572 Cretaceous times reflects the evolving oxygen fugacity of one or more magmatic systems,
573 probably located near the crust-mantle boundary. Corundum in cumulates that include Fe-
574 bearing silicates, Fe-Mg-Cr-Al spinels and Fe-Ni alloys crystallized at $f\text{O}_2 = \text{IW} \pm 1$, are zoned from
575 high-Cr cores to lower-Cr rims, consistent with fractional crystallization from a melt. The
576 reconstructed parental melts of such cumulates are Al-Cr-Fe-Mg-oxides. Cumulates that contain
577 Cr-Fe alloys, and which probably crystallized at somewhat lower $f\text{O}_2$, have low-Cr cores, and even
578 lower-Cr rims. However, corundum crystals that coexist with Cr^0 have crystallized near the
579 CrO/Cr^0 buffer ($f\text{O}_2 = \text{IW}-5$; Fig. 1a), and have low-Cr cores, but high-Cr rims (up to $>30\%$ Cr_2O_3).
580 These changes in zoning patterns reflect the strong relative decrease in the melting point of the
581 Cr_2O_3 end member with decreasing $f\text{O}_2$ (Fig. 16). EELS analyses show that all Cr in these corundum
582 crystals is present as Cr^{3+} , although most samples crystallized at or below the $f\text{O}_2$ of the Cr_2O_3 -CrO
583 buffer (Fig. 1a). This suggests that at least near the end of the evolution of these melts, Cr^{2+} in the
584 parental melt has disproportionated via the chemical reaction $3\text{Cr}^{2+}(\text{melt}) \rightarrow 2\text{Cr}^{3+}(\text{Crn}) + \text{Cr}^0$.

585 The most Cr-rich corundums have crystallized together with a range of β -alumina phases
586 including $\text{NaAl}_{11}\text{O}_{17}$ (diaoyudaoite), $\text{KAl}_{11}\text{O}_{17}$ (kahlenbergite) and β'' -alumina phases. From textural
587 evidence, these appear to have crystallized from melts, leaving residual melts that crystallized a
588 range of $(\text{K,Mg})_{1+x}\text{Al}_{11-x}\text{O}_{17}$ phases. The parental melts of these assemblages appear to have been
589 Al-Cr-K-Na-Mg oxides, which may be related to the Al-Cr-Fe-Mg oxide melts mentioned above
590 (Table 1), through either fractional crystallization or liquid immiscibility.

591 The samples described here cover a range in $f\text{O}_2$ from $\text{IW} \pm 1$ to $\text{IW}-5$, and thus are less
592 reduced than the assemblages in the melts trapped in the more abundant xenoliths of corundum
593 aggregates ($f\text{O}_2 = \text{IW}-6$ to -9 ; Griffin et al. 2019a). They are interpreted as representing an
594 intermediate stage in the $f\text{O}_2$ evolution of the hypothetical "ideal" magmatic system, in which
595 deep-seated evolving mafic magmas were fluxed by mantle-derived $\text{CH}_4 + \text{H}_2$ fluids (Griffin et al.
596 2018a). This is a newly recognized facet of the Mt Carmel assemblages, and helps to further
597 understand element partitioning under highly reducing conditions.

598 599 **Implications**

600 The zoning patterns of Cr in Cr-rich corundum crystals from Mt Carmel record changes in
601 the direction of fractional crystallization and the enrichment of Cr in oxide melts, controlled by a
602 decrease in fO_2 by five orders of magnitude during crystallization. This implies the supply of a
603 strongly reducing fluid to the magmas during crystallization, at high fluid/melt ratios. This in turn
604 provides a clear link to the still more reduced mineral assemblages trapped in the Cr-poor
605 corundum aggregates (Carmel Sapphire) found as xenoliths in the same volcanoes. Taken
606 together, these two groups of xenoliths define a magmatic system in which fO_2 decreased from *ca*
607 IW to IW-7 during the crystallization of the melts. The extremely low fO_2 reached toward the end
608 of this process (IW-9 to -10; Griffin et al. 2019a) requires a hydrogen-dominated environment, and
609 is strong evidence for the flux of mantle-derived CH_4+H_2 fluids at high melt-rock ratios during
610 basaltic eruptions over a period of 10-15 m.y. and an area of 150 km². This "mantle outgassing" is
611 a previously unrecognized process related to intraplate magmatism, with implications for the
612 oxidation state of the sublithospheric mantle and fluid transfer from mantle to crust.

613 Two different types of Al-rich oxide melts are represented by the samples described here,
614 one enriched in Fe, Ti, Zr and Cr, and the other enriched in Cr, Na and K; their common link is their
615 Cr content. This dichotomy suggests the development of liquid immiscibility during the evolution
616 of an original parental melt. Small-scale separation into silica-poor mafic melts enriched in HFSE
617 and transition elements, *versus* silica-alumina-rich melts that concentrate alkali elements, has
618 been noted in basaltic systems worldwide (e.g. Philpotts and Doyle 1983; Charlier et al. 2011;
619 Kamenetsky et al. 2013) and these processes may have operated at larger scales beneath Mt
620 Carmel. Oxide melts generated through liquid immiscibility are rarely erupted due to their high
621 density, and the unusual trapping of such melts in corundum aggregates at Mt Carmel may be
622 providing new insights into these processes.

623 624 **Acknowledgements**

625
626 We thank Paul Asimow and two anonymous referees for many useful comments and suggestions,
627 Dan Harlov for unbiased and constructive editorial handling, and Montgarri Castillo-Oliver for her
628 help with graphics. John Ward provided valuable insights into the nature and age of the alluvial
629 deposits. FC and DS acknowledge financial support from the Italian Ministry of Education (MIUR)
630 through the project "Dipartimenti di Eccellenza 2018–2022" for funding the installation of Raman
631 and single crystal X-ray diffraction facilities at Milan and a PhD grant for DS. LB thanks MIUR-
632 PRIN2017, project "TEOREM deciphering geological processes using Terrestrial and Extraterrestrial
633 ORE Minerals", prot. 2017AK8C32. WLG and SYO'R acknowledge the research funds for the TARDIS

634 Project provided by the ARC Centre of Excellence for Core to Crust Fluid Systems. We acknowledge
635 the scientific and technical assistance of Microscopy Australia at the Centre for Microscopy,
636 Characterization and Analysis, a facility funded by The University of Western Australia, and State
637 and Commonwealth Governments. Instruments used at Macquarie University are funded by DEST
638 Systemic Infrastructure Grants, ARC LIEF, NCRIS/AuScope, industry partners and Macquarie
639 University. This is contribution 1532 from the ARC Centre of Excellence for Core to Crust Fluid
640 Systems and 1405 from the GEMOC Key Centre.

641

642

643 **References**

644 Apter, D. (2014) High pressure indicator minerals from the Rakefet Magmatic Complex (RMC), Mt.
645 Carmel, Israel. in "Proceedings of the GSSA Kimberley Diamond Symposium", Extended
646 Abstract.

647 Beevers, C., and Ross, M. (1937) The crystal structure of beta alumina $\text{Na}_2\text{O}(\text{Al}_2\text{O}_3)_{11}$. Zeitschrift für
648 Kristallographie, 97, 59–66.

649 Bindi, L., Cámara, F., Griffin, W.L., Huang, J.-X., Gain, S.E.M., Toledo, V., and O'Reilly, S. (2019)
650 Discovery of the first natural hydride. *American Mineralogist*, **104**, 611–614.

651 Birnie, D.P. (2012) On the structural integrity of the spinel block in the β "-alumina structure. *Acta*
652 *Crystallographica*, B68, 118–122.

653 Bowen, N.L. (1912) The binary system: $\text{Na}_2\text{Al}_2\text{Si}_2\text{O}_8$ (nephelite, carnegieite)- $\text{CaAlSi}_3\text{O}_8$ (anorthite).
654 *American Journal of Science*, S4, 33, 551–573.

655 Bravo, B.O., Griffin, W.L., Gain, S.E.M., Saunders, M., Shaw, J., Toledo, V. Afonso, J.C., and O'Reilly,
656 S.Y. (2020). Ti³⁺ in corundum: tracing crystal growth in a highly reduced magma. *Scientific*
657 *Reports*, in press.

658 Charlier, B., Namur, O., Toplis, M.J., Schiano, P., Cluzel, N., Higgins, M.D., and Van der Auwera, J.
659 (2011) Large-scale silicate liquid immiscibility during differentiation of tholeiitic basalt to
660 granite and the origin of the Daly gap. *Geology*, 39, 907–910.

661 Colomban, Ph., and Lucazeau, G. (1980) Vibrational study of conduction mechanism in β alumina.
662 I. Stoichiometric β alumina. *Journal of Chemical Physics*, 72, 1213–1224.

663 Degterov, S., and Pelton, A.D. (1996) Critical evaluation and optimization of the thermodynamic
664 properties and phase diagrams of the CrO-Cr₂O₃, CrO-Cr₂O₃-Al₂O₃ and CrO-Cr₂O₃-CaO
665 systems. *Journal of Phase Equilibria*, 17, 476–487.

- 666 Dernier, P.D., and Remeika, J.P. (1976) Structural determinations of single-crystal K beta-alumina
667 and cobalt-doped K beta-alumina. *Journal of Solid State Chemistry*, 17, 245–253.
- 668 Donovan, J.J., and Tingle, T.N. (1996) An improved mean atomic number background correction
669 for quantitative microanalyses. *Journal of Microscopy and Microanalysis*, 2(1), 1–7.
- 670 Donovan, J.J., Singer, J.W., and Armstrong, J.T. (2006) A new EPMA method for fast trace element
671 analysis in simple matrices. *American Mineralogist*, 101, 1839–1853.
- 672 Edström, K., Thomas, J.O., and Farrington, G. C. (1991) Structural aspects of the Na⁺ → Cd²⁺ ion-
673 exchange process in Na⁺ β-alumina. *Acta Crystallographica*, B47, 635–643.
- 674 Farrington, G.C., and Dunn, B. (1982) Divalent beta"-aluminas: high conductivity solid electrolytes
675 for divalent cations. *Solid State Ionics*, 7, 267–281.
- 676 Fukai, Y. 2005. *The Metal-Hydrogen system*. Springer, Berlin. 505 pp.
- 677
- 678 Giuliani, G., Pivin, M., Fallick, A.E., Ohnestetter, D., Song, Y., and Demaiffe, D. (2015) Geochemical
679 and oxygen isotope signatures of mantle corundum megacrysts from the Mbuji-Mayi
680 kimberlite, Democratic Republic of Congo, and the Changle alkali basalt, China. *Comptes*
681 *Rendus Geoscience*, 347, 24–34.
- 682 Grapes, R., and Palmer, K. (1996) (Ruby-sapphire)-chromian mica-tourmaline rocks from
683 Westland, New Zealand. *Journal of Petrology*, 37, 293–315.
- 684
- 685 Griffin, W.L., Gain, S.E.M., Adams, D.T., Huang, J-X., Saunders, M., Toledo, V., Pearson, N.J., and
686 O'Reilly, S.Y. (2016) First terrestrial occurrence of tistarite (Ti₂O₃): Ultra-low oxygen
687 fugacity in the upper mantle beneath Mt Carmel, Israel. *Geology*, 44, 815–818.
- 688
- 689 Griffin, W.L., Huang, J-X., Thomassot, E., Gain, S.E.M., Toledo, V., and O'Reilly, S.Y., (2018a) Super-
690 reducing conditions in ancient and modern volcanic systems: Sources and behaviour of
691 carbon-rich fluids in the lithospheric mantle. *Mineralogy and Petrology*, 112, Supp. 1, 101–
692 114.
- 693
- 694 Griffin, W.L., Gain, S.E.M., Bindi, L., Toledo, V., Cámara, F., Saunders, M., and O'Reilly, S.Y. (2018b)
695 Carmeltazite, ZrAl₂Ti₄O₁₁, a new mineral trapped in corundum from volcanic rocks of Mt
696 Carmel, northern Israel. *Minerals*, 8, 601–612.
- 697
- 698 Griffin, W.L., Gain, S.E.M., Huang, J-X., Saunders, M., Shaw, J., Toledo, V., and O'Reilly, S.Y. (2019a)
699 A terrestrial magmatic hibonite-grossite-vanadium assemblage: desilication and extreme
700 reduction in a volcanic plumbing system, Mt Carmel, Israel. *American Mineralogist*, 104,
701 207–219.
- 702
- 703 Griffin, W.L., Toledo, V., and O'Reilly, S.Y. (2019b) Discussion of “Enigmatic super-reduced phases
704 in corundum from natural rocks: Possible contamination from artificial abrasive materials or
705 metallurgical slags” by Litasov et al. (2019). *Lithos*, 348–349, 105122.
- 706

- 707 Griffin, W.L., Gain, S.E.M., Saunders, M., Bindi, L., Alard, O., Toledo, V., and O'Reilly, S.Y. (2020a)
708 Parageneses of TiB₂ in corundum xenoliths from Mt Carmel, Israel: Siderophile behaviour of
709 Boron under reducing conditions. American Mineralogist, in press.
710
711 Griffin, W.L., Gain, S.E.M., Cámara, F., Bindi, L., Shaw, J., Alard, O., Saunders, M., Huang, J-X.,
712 Toledo, V., and O'Reilly, S.Y. (2020b) Extreme reduction: Mantle-derived oxide xenoliths
713 from a hydrogen- rich environment. Lithos, 358–359, 105404.
714
715 Harries, D., and Langenhorst, F. (2011) Nanocrystalline P-bearing pentlandite and chromium
716 nitrides from CM2 chondrites Y-791198 and Y-793321. 74th Annual Meeting of the
717 Meteoritical Society. Meteoritics & Planetary Science, 46, Supplement, A88.
718
719 Huang, J-X., Xiong, Q., Gain, S.E.M., Murphy, T.D., Griffin, W.L., Shiryaev, A.A., Toledo, V., Tomshin,
720 M.D., and O'Reilly, S.Y. (2020) Immiscible metallic melts in the deep Earth: clues from
721 moissanite (SiC) in volcanic rocks. Science Bulletin, 65, 1479-1488.
722
723 Hutchinson, M.T., Nixon, P.H., and Harley, S.L. (2004) Corundum inclusions in diamonds -
724 discriminatory criteria and a corundum compositional dataset. Lithos, 77, 273–286.
725
726 Janak, M., Uher, P., Ravna E. K., Kullerud, K., and Vrabec, M. (2015) Chromium-rich kyanite,
727 manesiostauroilite and corundum in ultrahigh-pressure eclogites (examples from Pohorje
728 Mountains, Slovenia and Tromsø Nappe, Norway. European Journal of Mineralogy, 27, 377–
729 392.
730
731 Jung, I-H., Degterov, S., and Pelton, A.D. (2005) Thermodynamic modeling of the MgO-Al₂O₃-CrO-
732 Cr₂O₃ system. Journal of American Ceramic Society, 88, 1921–1928.
733
734 Jackson, S.E., Pearson, N.J., Griffin, W.L. and Belousova, E.A. 2004. The application of laser
735 ablation-inductively coupled plasma-mass spectrometry to in-situ U-Pb zircon
736 geochronology. Chemical Geology, 211, 47–69.
737
738 Kamenetsky, V.S., Charlier, B., Zhitova, L., Sharygin, V., Davidson, P.I., and Feig, S. (2013) Magma
739 chamber-scale liquid immiscibility in the Siberian Traps represented by melt pools in native
740 iron. Geology, 41, 1091–1094.
741
742 Kaminchik, J., Segev, A., and Katzir, Y. (2014). The origin of intraplate alkaline mafic magmatism in
743 continental shelves: lavas and xenoliths from the Upper Cretaceous volcanos of Mt Carmel.
744 Geological Survey of Israel report GSI/19/2014, 45 pp. in Hebrew with extended English
745 abstract.
746
747 Kim, D-G., Moosavi-Khoonsari, E. and Jung, I-H. (2018) Thermodynamic modeling of the K₂O-Al₂O₃
748 and K₂O-MgO-Al₂O₃ systems with emphasis on β- and β''-aluminas. Journal of European
749 Ceramic Society, 38, 3188–3200.
750

- 751 Krüger, B. (2019) Kahlenbergite, a new potassium β -alumina mineral. Abstract at the 32nd
752 European Crystallographic Meeting, Vienna, August 2019.
753
- 754 Krüger, B., Galuskin, E.V., Galuskina, I.O., Krüger, H., and Vapnik, Y. (2019) Kahlenbergite, IMA
755 2018-158. CNMNC Newsletter No. 49, June 2019. Mineralogical Magazine, 83, 323–328.
756
- 757 Krzanowski, J.E., and Foley, D.J. (2014) The effect of Cr content on the oxidation behaviour of Ti-
758 Cr-N films. Coatings, 4, 308–319.
759
- 760 Litasov, K.D., Kagi, H. and Bekker, T.B. (2019a) Enigmatic super-reduced phases in corundum from
761 natural rocks: Possible contamination from artificial abrasive materials or metallurgical slags.
762 Lithos 340-341, 181-190.
763
- 764 Litasov, K.D., Bekker, T.B. and Kagi, H. (2019b) Reply to the discussion of “Enigmatic super-
765 reduced phases in corundum from natural rocks: Possible contamination from artificial
766 abrasive materials or metallurgical slags” by *Litasov et al.* (Lithos, v.340–341, p.181–190) by
767 W.L. Griffin, V. Toledo and S.Y. O'Reilly. Lithos 348-349, 105170.
768
- 769 Lyutaya, M.D., and Kulik, O.P. (1974) Some characteristics of the formation of chromium nitrides.
770 Soviet Powder Metall. Metal Ceramics, 13, 792–794.
771
- 772 McBride, S.P., and Brydson, R. (2004) Analytical transmission electron microscopy and surface
773 spectroscopy of ceramics: The microstructural evolution in titanium-doped chromia
774 polycrystals as a function of sintering conditions. Journal of Material Science 39(22), 6723-
775 6734.
776
- 777 Mittlefehldt, D.W. (1986) Petrology of high pressure clinopyroxenite series xenoliths, Mount
778 Carmel, Israel. Contributions to Mineralogy and Petrology 94, 245-252.
779
- 780 Papike, J. J., Simon, S.B., Burger, P.V., Bell, A.S., Shearer, C.K., and Karner, J.M. (2016) Chromium,
781 vanadium and titanium valence systematics in solar system pyroxene as a recorder of
782 oxygen fugacity, planetary provenance, and processes. American Mineralogist, 101, 907–
783 918.
784
- 785 Philpotts, A.R., and Doyle, C.D. (1983) Effect of magma oxidation state on the extent of silicate
786 liquid immiscibility in a tholeiitic basalt. American Journal of Science, 283, 967–986.
787
- 788 Richet, P., and Mysen, B.O. (1999) High-Temperature dynamics and Carnegiteite (NaAlSiO₄): in
789 cristobalite (SiO₂): a Raman Spectroscopy study. Geophysical Research Letters, 26(15), 2283–
790 2286.
791
- 792 Sass, E. (1980) Late Cretaceous volcanism in Mount Carmel, Israel. Israel Journal of Earth Sciences,
793 29, 8-24.
794

- 795 Schaeffer, G.W., Van Zyl, A., and Weppner, W. (1990) Direct synthesis of divalent Beta-alumina
796 and related phases. *Solid State Ionics*, 40/41, 154–157.
- 797
798 Schreiber, H.D., and Haskin, L.A. (1976) Chromium in basalts: Experimental determination of redox
799 states and partitioning among synthetic silicate phases. *Proceedings of the 7th Lunar and*
800 *Planetary Science Conference*, 1221–1259.
- 801
802 Segev, A., and Rybakov, M. (2011) History of faulting and magmatism in the Galilee (Israel) and
803 across the Levant continental margin inferred from potential field data. *Journal of*
804 *Geodynamics*, 51, 264-284.
- 805
806 Shen, S., Chen, L., Li, A., Dong, T., Huang, Q., and Xu, W. (1986) Diaoyudaoite - a new mineral. *Acta*
807 *Mineralogica Sinica*, 6, 224–227 (in Chinese with English abstract).
- 808
809 Sheldrick, G.M. (2015) Crystal structure refinement with SHELXL. *Acta Crystallographica*, C71, 3–8.
- 810
811 Sinmyo, R., Hirose, K., and Ohishi, Y. (2019). Melting curve of iron to 290 GPa determined in a
812 resistance-heated diamond-anvil cell. *Earth and Planetary Science Letters*, 510, 45-52.
- 813 Smith, E.M., Shirey, S.B., Nestola, F., Bullock, E.S., Wang, J., Richardson, S.H., and Wang, W. (2016)
814 Large gem diamonds from metallic liquid in Earth's deep mantle. *Science*, 354, 1403–1405.
- 815
816 Smith, E.M., Shirey, S.B., Richardson, S.H., Nestola, F., Bullock, E.S., Wang, J., and Wang, W. (2018)
817 Blue boron-bearing diamonds from Earth's lower mantle. *Nature*, 560, 84–87.
- 818
819 Stein, M. and Goldstein, S.L. (1996) From plume head to continental lithosphere in the Arabian-
820 Nubian shield. *Nature*, 382, 773-778.
- 821
822 Stein, M. and Hofmann, A.W. (1992) Fossil plume head beneath the Arabian lithosphere? *Earth*
823 *and Planetary Science Letters*, 114, 193-209.
- 824
825 Sutherland, F.L., Zaw, K., Meffre, S., Giuliani, G., Fallick, A.E., Graham, I.T., and Webb, G.B. (2009)
826 Gem-corundum megacrysts from east Australian basalt fields: trace elements, oxygen
827 isotopes and origins. *Australian Journal of Earth Science*, 56, 1003–1022.
- 828
829 Watt, G.R., Harris, J.W., Harte, B., and Boyd, S.R. (1994) A high-chromium corundum (ruby)
830 inclusion in diamond from the Sao Luiz alluvial mine, Brazil. *Mineralogical Magazine*, 58,
831 490–493.
- 832
833 Wilson, A.J.C. (editor) (1992) *International Tables for Crystallography*. Volume C: Mathematical,
834 physical and chemical tables. Kluwer Academic Publishers, Dordrecht, The Netherlands.
- 835
836 Xiong, Q., Griffin, W.L., Huang, J-X., Gain, S.E.M., Toledo, V., Pearson, N.J., and O'Reilly, S.Y. (2017)
837 Super-reduced mineral assemblages in “ophiolitic” chromitites and peridotites: The view
838 from Mt Carmel. *European Journal of Mineralogy*, 29, 557–570.
- 839

840 Yaxley, G.M., Berry, A.J., Kamenetsky, V.S., Woodland, A.B., Golovin, A.V. (2012) An oxygen
841 fugacity profile through the Siberian Craton — Fe K-edge XANES determinations of $\text{Fe}^{3+}/\Sigma\text{Fe}$
842 in garnets in peridotite xenoliths from the Udachnaya East kimberlite. *Lithos*, 140-141, 142–
843 151.

844
845

846 **Figure Captions**

847

848 Figure 1. (a) oxidation state ($\log f\text{O}_2$ relative to IW buffer) represented by various redox reactions
849 recorded in the xenolith suite. After Papike et al. (2016). (b) Evolution of an idealized magmatic
850 system beneath Mt Carmel, in which an evolved mafic/syenitic melt is fluxed by mantle-derived
851 CH_4+H_2 fluids. The reconstructed succession of key mineral associations is based on xenoliths in
852 the tuffs of the Cretaceous volcanoes, while their respective oxidation states are derived from
853 observed redox reactions and/or dominance of specific valence states of Fe, Cr, Ti and V.

854

855 Figure 2. Maps summarizing regional setting and geological information, including the locations of
856 Cretaceous volcanic centers and main alluvial deposits.

857

858 Figure 3. (a) The black massive pyroclastic rocks in Vent #1 of the Rakefet Magmatic Complex;
859 geological hammer for scale. White clasts are from the country-rock limestones; (b), closer view
860 of massive pyroclastics in the Rakefet Magmatic Complex.

861

862 Figure 4. (a) Variegated pyroclastics from the Rakefet Magmatic Complex, showing layering of
863 coarse and fine lapilli, xenoliths and xenocrysts, with carbonate cement; (b) Polished slab of the
864 variegated pyroclastics from the Rakefet Magmatic complex.

865

866 Figure 5. (a) Back-scattered electron (BSE) image of sample 1174-1A. Most of the sample appears
867 to be a cumulate of touching corundum prisms, with high-Cr cores (to 15 wt% Cr_2O_3) and lower-Cr
868 (ca 10 wt% Cr_2O_3) rims. The barred area in the lower part of the grain is interpreted as the
869 crystallization products of a eutectic melt (see Table 1). (b) Element maps and multi-element
870 phase map of the grain. Mg map is dominated by an interstitial Fe-Mg-Cr-Al spinel.

871

872 Figure 6. (a) Close-up BSE image of the barred area in sample 1174-1A, showing texture
873 interpreted in terms of eutectic crystallization. (b) Element maps and layered-EDS phase map
874 showing the distribution of individual phases.

875

876 Figure 7. BSE images and ELEMENT maps of possible corundum cumulates or skeletal crystals
877 (Table 2). (a) BSE image of sample 1210B-4, with corundum prisms zoned from higher-Cr cores
878 (2.5 wt% Cr₂O₃ to lower-Cr (ca 1 wt%) rims; matrix is dominated by Na-β-alumina (diaoyudaoite);
879 metallic droplets are a Cr-Fe-Ga alloy. (b) BSE image of sample 1210B-5 showing blocky corundum
880 crystals with high-Cr cores (6.7% wt% Cr₂O₃) and Cr-poor rims (0.4 wt% Cr₂O₃); matrix is K-β-
881 alumina (kahlenbergite), metallic droplets are Cr⁰. (c) BSE image, layered-EDS map and element
882 maps of sample 1125-2D. The texture suggests a cumulate of corundum prisms with low-Cr cores
883 (ca 4 wt% Cr₂O₃) and Cr-rich rims (27 wt% Cr₂O₃). Interstitial material is a K-β-alumina, some as
884 apparently lath-shaped crystals; metallic droplets are Cr⁰.

885

886 Figure 8. Images of sample 1174C. (a) BSE image and transmitted-light photomicrograph showing
887 colour, and distribution of highest-Cr parts (light areas in BSE). Note ball of Cr⁰ on edge of crystal.
888 (b) 3D oblique SEM-view with overlain layered-EDS map of the surface of 1174C before sectioning.
889 Rough dark green in lower part of the image is the ruby; smooth dark green in the upper part is
890 the K-β-alumina. Small bright grains along rim of crystal in middle of image are Ni-bearing Fe⁰.
891 Bright pink-purple "mushrooms" are Cr⁰. (c) Layered-EDS map and Al distribution map of the
892 contact between the largest Cr sphere, showing higher Cr (lower Al) toward the Cr ball, and the
893 compositional granularity of the high-Cr zone. Red line shows location of FIB foil. Note granularity
894 in the Cr and Al maps of the corundum, interpreted as the result of spinodal breakdown. (d) TEM-
895 BSE image and element maps of FIB foil across contact between Cr⁰ and Cr-rich corundum,
896 separated by a zone of Cr₂N.

897

898 Figure 9. EELS spectra of corundum, Cr-nitride and Cr⁰ from the FIB foil shown in Fig. 5d. The
899 shifts in Cr peak positions indicate that Cr is present in both high-Cr and low-Cr corundum as Cr³⁺,
900 and in the nitride as Cr²⁺, or a mixture of Cr²⁺ and Cr¹⁺.

901

902 Figure 10. Incident-light photograph (rough stone) and BSE image (after polishing) of sample
903 1175A. The light grey material veining the corundum and surrounded by high-Cr (8% Cr₂O₃)
904 corundum is a K,Mg-β-alumina (Table 3). The large metallic grain (inset) is divided 60:40 between
905 darker Cr⁰ and lighter Cr_{1.3}N.

906

907 Figure 11. Images of individual corundum grains with abundant Cr⁰. (a) Optical (rough stones) and
908 BSE images (polished samples) of samples 1210A-1 (right) and 1210A-2 (left). Dark cores of

909 corundum contain <0.5 wt% Cr₂O₃, while lighter zones contain 10-12 wt%. Cr⁰ droplets are mostly
910 associated with a K-β"-alumina (Table 4). (b) BSE image of sample 1210B-1, showing possible
911 skeletal structure. Dark corundum contains 6 wt% Cr₂O₃, while light rims have >35 wt%. Metallic
912 grains are a Cr-Fe-Ga alloy. Laths of K-β"-alumina are overgrown by K-β"-alumina with 17-18%
913 Cr₂O₃. (c) BSE image of sample 1210B-3 with possible skeletal structure. Dark corundum cores
914 contain <1 wt% Cr₂O₃, and lighter rims ca 7 wt %. Metallic grains are Cr⁰, and mostly occur within a
915 matrix of K,Mg-β"-alumina (Table 4).

916

917 Figure 12. Phase diagram of the Cr-N system, showing relationships of the CrN (FCC) and Cr₂N
918 (HCP) phases. Data from SGTE 2007 alloy database; see also
919 http://www.crct.polymtl.ca/fact/documentation/SGTE2017/SGTE2017_Figs.htm

920

921

922 Figure 13. Phase diagram for the K₂O-Al₂O₃ binary, showing compositions of the alumina phases
923 analyzed in this work. After Kim et al. (2018).

924

925 Figure 14. Liquidus diagram for the MgO-K₂O-Al₂O₃ ternary, showing compositions of the alumina
926 phases analyzed in this study. Symbols correspond to populations shown on Figure 13. After Kim
927 et al. (2018).

928

929 Figure 15. Liquidus-solidus-subsolidus relationships in the Al₂O₃ (corundum)-Cr₂O₃ (eskolaite)
930 binary at 1 atm. Cr# = molar Cr/(Cr+Al). Vertical black bars mark compositions of coexisting
931 phases in the granular texture shown in Figure 8. After Degterov and Pelton (1996).

932

933 Figure 16. Evolution of the liquidus-solidus loop in the corundum-eskolaite (Cr₂O₃) binary with
934 decreasing *f*O₂. At high *f*O₂ a crystallizing oxide has higher Cr/Al than the coexisting melt; at lower
935 *f*O₂ this relationship is reversed, because the melting point of the Cr-oxide drops with decreasing
936 *f*O₂, while the melting point of Al₂O₃ remains constant. After Degterov and Pelton (1996). Tie
937 lines connect mean cores, rims and overgrowths of corundum crystals in individual samples. Some
938 rims approach the predicted Cr/Al of the melt coexisting with the core of the grain, but most rims,
939 and all overgrowths, have higher Cr/Al than the predicted melts, implying further fractional
940 crystallization and probably lower temperatures. For the fixed *P*_{O₂} values of each panel, the *f*O₂

941 relative to IW varies over the temperature range of crystallization: (a) IW +1 to +2; (b) *ca* IW; (c) *ca*
942 IW-2; (d) IW-3 to IW-4.

943

944 **Supplementary Data**

945

946 Figure SD-1. A source-to-sink geological model showing the 3-fold division of the Kishon River
947 catchment (3D view, not to scale). Two of the Cretaceous volcanoes, Rakefet (RMC) and
948 Muharaka are shown to illustrate their situation high above the valley. Cretaceous volcanic
949 centers in red, Cover Basalts in pink and Miocene basalts in purple. Recovered indicator minerals:
950 C, corundum; M, moissanite; H, hibonite; D, diamond. The recovery of corundum and other
951 minerals from the cover basalts is inferred from drainage sampling. However, these occurrences
952 also coincide with the maximum extent of Miocene beach deposits, which may be the source of
953 the alluvial minerals.

954

955 Figure SD-2. (a) Typical stratigraphic section (sample BS1253) of a terrace above the Kishon River,
956 with paleo-placers confined to the coarser basal stratum (site BS1253; green box); (b) Selected
957 minerals recovered from BS1253 (333 tons of gravel processed).

958

959 Figure SD-3. Rubies (0.3-1 mm fraction) separated from vent tuffs of the Rakefet Magmatic
960 Complex (bulk sample SY-479); Cr₂O₃ contents are 1.5-2 wt%. Cf Figure 11.

961

962 Figure SD-4. Binocular-microscope photo of typical Miocene carbonate-cemented beach placer
963 (Shefa Yamim Sample SY-186, collected in 2003) from near Migdal-Ha-Emec (Figure SD-1). Note
964 abundant moissanite and garnet (orange). Scale is in mm.

965

966 Figure SD5. Raman spectrum of the NaAlSiO₄ phase in sample 1174A-1 (Figs 5,6) compared with
967 the spectrum of the synthetic phase (“carnegieite”). The Raman spectrum was collected on
968 NaAlSiO₄ grains (532 nm laser, 20 sec acquisition, 32.25 nW). Light blue peaks are Gaussian fit
969 (fitted peak positions reported on top). The spectrum of carnegieite at 298 K (488 nm argon ion
970 laser, 100 sec acquisition, 500 mW) modified from figure 1 of Richet and Mysen (1999) is shown as
971 a dashed line for comparison. While a few peaks have close Raman shifts, it is evident that the
972 spectra correspond to two different phases.

973

974 Figure SD6. Raman spectrum of kahlenbergite from sample 1210B-1 (Fig. 7b) compared with the
975 spectrum of the synthetic material. The Raman spectrum was collected on a kahlenbergite from
976 grain 1210B-1 (532 nm laser, 20 sec acquisition, 32.25 nW). Light blue peaks are Gaussian fit (fitted
977 peak positions reported on top). The spectrum of Na- β -alumina at 20 K (488 nm argon ion laser)
978 modified from figure 3b of Colomban and Lucazeau (1980) is shown as a dashed line for
979 comparison. The match is good considering the difference in composition (K instead of Na) and
980 temperature.

981
982 Table SD-1. Xenocryst minerals recovered from pyroclastic rock samples from individual
983 Cretaceous volcanic centers, Mt Carmel.

984
985 Appendix: Sampling, Analytical methods
986 CIF files of diaoyudaoite 1210B4-1b and kahlenbergite 1210B1-1b
987

Table 1. Analytical data for sample 1174-1A

Fe-Ni alloy			corundum		spinel		
		wt %	cores	rims	SEM		EMP
n=3			n=2	n=5	n=12	stdev	n=8
Si	0.07	SiO ₂	0.02	0.06			0.11
Al	0.04	ZrO ₂	0.00	0.00			0.01
Cr	0.92	TiO ₂	0.19	0.62	0.31	0.19	0.36
Mn	0.00	Al ₂ O ₃	84.52	87.6	52.26	2.29	52.64
Fe	87.64	Cr ₂ O ₃	14.76	10.32	12.8	0.95	11.38
Ni	10.28	V ₂ O ₅	0.03	0.05			0.02
P	0.28	FeO	0.08	0.14	11.8	0.82	11.45
total	98.95	NiO	n/a	n/a			n/a
		MnO	0.08	0.02			0.16
at. %		MgO	0.00	0.22	20.2	1.42	20.96
Si	0.13	CaO	0.01	0.00			0.01
Al	0.08	Na ₂ O	0.00	0.00			0.04
Cr	1.01	K ₂ O	0.00	0.00			0.00
Mn	0.00	total	99.69	99.03	97.37		97.28
Fe	88.6						
Ni	9.71						
P	0.48	at.%					
		Si		0.03			0.04
		Zr					
		Ti	0.05	0.17	0.09	0.05	0.10
		Al	35.7	36.73	23.70	0.19	22.09
		Cr	4.37	2.90	3.78	0.32	3.20
		V	0.01	0.02			0.01
		Fe	0.02	0.04	3.70	0.23	3.41
		Ni					
		Mn	0.02				0.05
		Mg		0.12	11.80	0.41	11.12
		Ca					0.01
		Na					
		O	60.00	60.00	56.90	0.11	60.00
		Cr#	0.109	0.073	0.14		0.13

	K-free nepheline		(Fe,Mg,Ni)(Al,Cr) ₂ O ₄		Zr ₂ O ₃	(Na,Fe,Mg) ₂ (Al,Ti,Cr) ₆ O ₁₁			
	SEM	EMP	SEM	EMP	SEM	SEM		EMP	
	n=7	n=5	n=5	n=1	n=3	n=11	stdev	n=11	stdev
SiO ₂	41.7	43.66		0.03				0.51	0.24
ZrO ₂		0.00		0.00	82.40	1.21	0.41	1.22	0.35
TiO ₂	0.15	0.42	0.55	0.39	3.16	14.10	2.43	13.05	1.52
Al ₂ O ₃	34.50	37.64	42.30	43.41	3.24	48.80	3.32	51.30	2.11
Cr ₂ O ₃	0.18	0.62	14.9	16.46	0.69	7.37	0.68	7.61	0.05
V ₂ O ₅		0.05		0.05				0.19	0.02
FeO	0.85	1.14	36.10	36.89	0.75	13.3	0.83	13.10	0.67
NiO		n/a	1.56	0.03				n/a	
MnO		0.024						0.01	0.08
MgO		0.47	0.97	1.31		3.94	0.28	4.10	0.13
CaO	0.22	0.30		0.01		2.33	1.15	2.81	0.97
Na ₂ O	17.10	14.18		0.01	0.17	2.21	0.74	2.17	
K ₂ O		0.17		0.00				0.01	
total	94.75	98.66	96.37	98.56	90.38	93.21		94.90	
at.%									
Si	14.29	14.76						0.20	0.23
Zr					28.5	0.26	0.08	0.23	0.10
Ti	0.04	0.12	0.15	0.13	1.68	4.46	0.75	3.87	0.89
Al	13.93	15.00	21.70	21.03	2.68	24.20	1.21	23.82	1.60
Cr	0.05	0.17	5.30	5.35	0.39	2.45	0.17	2.37	0.29

V								0.06	0.01
Fe	0.24	0.32	13.00	12.68	0.44	4.68	0.27	4.32	0.37
Ni			2.40	0.01					
Mn								0.00	0.01
Mg		0.24	0.57	0.80		2.47	0.10	2.31	0.17
Ca	0.08	0.11				1.05	0.52	1.69	0.60
Na	11.36	9.29				1.80	0.59		
O	60.0	60.0	56.80	60.00	66.30	58.60	0.04	61.10	
Cr#			0.20	0.20	0.13	0.09		0.09	

	(Fe,Mg)(Al,Cr,Ti,Si) ₈ O ₁₃	Reconstruction (Fig. 2)		
	EMP	barred	coarse	whole
	<i>n</i> =4	area	area	grain
SiO ₂	3.02	2.1	1.1	1.7
ZrO ₂	0.00	0.0	0.0	0.2
TiO ₂	0.58	1.7	1.1	1.7
Al ₂ O ₃	75.46	77.6	81.8	77.5
Cr ₂ O ₃	5.19	8.4	9.4	8.2
V ₂ O ₅	0.01	0.0	0.0	0.1
FeO	6.98	4.6	2.9	4.5
NiO	n/a	0.0	0.0	0.0
MnO	0.08	0.0	0.0	0.0
MgO	4.18	4.3	3.0	4.5
CaO	0.01	0.2	0.1	0.2
Na ₂ O	0.25	1.1	0.6	1.3
K ₂ O	0.05			
total	95.81	100.0	100.0	100.0
at. %				
Si	1.48			
Zr	0.01			
Ti	0.35			
Al	39.87			
Cr	3.58			
V	0.01			
Fe	5.37			
Ni				
Mn	0.07			
Mg	2.55			
Ca	0.01			
Na	0.20			
O	42.4			

Table 2. Analytical data for corundum "cumulates"

wt %	1210B-4				1210B-5				1125-2D								
	corundum			β-alumina	Cr-alloys			β-alumina	corundum		Cr-alloy	β-alumina	corundum			Cr alloy	
	cores	rims	outer	Na-Cr	wt%	SEM			cores	rims			cores	rims	outer		
<i>n</i> =3	<i>n</i> =3	<i>n</i> =3	<i>n</i> =3		<i>n</i> =2	<i>n</i> =1	<i>n</i> =1	<i>n</i> =3	<i>n</i> =6	<i>n</i> =4	<i>n</i> =3	<i>n</i> =5	<i>n</i> =4	<i>n</i> =3	<i>n</i> =2	<i>n</i> =2	
SiO2	0.02	0.01	0.02	0.07	Si	0.10	0.06	0.05	0.00	0.02	0.01	0.04 (Si)	0.01	0.02	0.02	0.00	0.11
ZrO2	0.01	0.00	0.00	0.02	Cr	51.68	49.69	78.89	0.00	0.00	0.00	0.01	0.00	0.00	0.00	0.02	
TiO2	0.01	0.01	0.01	0.01	Fe	44.78	46.12	16.68	0.00	0.00	0.01	0.00	0.00	0.00	0.01	0.13	
Al2O3	97.63	98.39	94.29	88.06	Ga	2.76	n/a	n/a	87.25	99.65	94.02	0.15 (Al)	85.96	96.27	72.38	64.62	0.07
Cr2O3	2.17	1.26	5.33	4.40	total	99.31	95.87	95.62	1.96	0.40	6.07	99.47(Cr)	2.97	3.78	27.05	34.19	99.5
V2O3	0.00	0.01	0.00	0.00					0.00	0.00	0.00	0.00	0.00	0.01	0.03	0.04	
FeO	0.02	0.01	0.00	0.02	at.%				0.00	0.01	0.00	0.00	0.00	0.00	0.00	0.00	
MnO	0.00	0.01	0.03	0.01	Si	0.20	0.12	0.1	0.00	0.02	0.01	0.27(Mn)	0.02	0.02	0.07	0.06	0.23
MgO	0.00	0.01	0.00	0.34	Cr	53.89	53.58	83.47	1.39	0.03	0.01	0.00	0.06	0.00	0.00	0.02	
CaO	0.00	0.00	0.01	0.14	Fe	43.47	46.30	16.43	0.08	0.00	0.00	0.00	0.02	0.01	0.01	0.01	
Na2O	0.00	0.00	0.00	5.01	Ga	2.14			0.06	0.00	0.01	0.02	0.07	0.01	0.01	0.02	
K2O	0.00	0.00	0.01	0.21					7.17	0.00	0.01	0.00	11.50	0.00	0.01	0.02	
total	99.81	99.69	99.68	93.30					97.88	100.13	100.10	99.99	100.6	100.1	99.6	99.11	100.00
at %																	
Si	0.01		0.01	0.02								0.09		0.01	0.01		0.20
Zr																	
Ti																0.04	
Al	39.4	39.65	38.53	36.51					35.31	39.88	38.33	0.29	34.17	38.94	31.92	29.46	0.13
Cr	0.59	0.34	1.46	1.22					0.54	0.11	1.66	99.38	0.79	1.03	8.00	10.46	99.47
V															0.01	0.01	
Fe																	
Ni																	
Mn												0.26			0.02	0.02	0.19
Mg				0.18					0.72				0.03		0.03	0.01	
Ca				0.04					0.03				0.01				
Na				3.42									0.05				
K				0.09					3.16				4.95				
O	60.0	60.0	60.0	58.6					63.4	60.0	60.0		65.0	60.0	60.0	60.0	
Cr#	0.01	0.01	0.04	0.03					0.02	0.003	0.042		0.02	0.026	0.200	0.262	

Table 3. Analytical data for two large hopper crystals of corundum

1174C								
corundum								
in contact with Cr balls						cores		main
	SEM		EMP	TEM		SEM	EMP	
wt. %	n=9	stdev	n=3	low-Cr	high-Cr	n=3	n=3	n=6
SiO ₂			0.01				0.00	0.01
ZrO ₂			0.00				0.00	0.00
Ti ₂ O ₃			0.00				0.00	0.01
Al ₂ O ₃	68.6	9.0	68.90	70.4	42.2	97.0	97.08	76.80
Cr ₂ O ₃	31.4	3.3	31.15	29.7	57.6	2.95	2.95	23.14
V ₂ O ₃			0.02				0.00	0.02
FeO			0.00				0.00	0.00
MnO			0.04				0.02	0.05
MgO			0.01				0.00	0.01
CaO			0.00				0.00	0.02
total	100.0		100.14	100.1	99.8	100.0	100.1	100.0
at. %								
Al	30.6		30.6	31.2	20.8	39.2	39.2	33.3
Cr	9.41		9.29	8.84	19.1	0.80	0.80	6.72
V			0.01					0.01
Mn			0.01					0.02
Mg			0.01					0.01
Ca								
O	60.0		60.0	59.9	60.1	60.0	60.0	60.0
Cr#	0.24		0.23	0.22	0.48	0.02	0.02	0.17
ppm	(LA-ICPMS)							
Mg			98					17
Si			1405					1460
P			42					29
Sc			<0.9					<0.4
Ti			58					3
V			156					34
Cr			166000					13800
Fe			<28					<20
Co			<0.12					<0.03
Ni			<0.63					<0.12
Zn			<0.93					<0.75
Ga			0.22					<0.05
Zr			3.4					0.11
Nb			0.07					0.11

1174c (cont.)							
wt. %	β-alumina	spinel	% element	Cr balls		Cr nitride	
	n=4	n=4		SEM	EMP	SEM	TEM
	n=4	n=4		n=8	n=3	n=2	
			N			7.69	13.2
SiO ₂	0.02	0.01	Si	0.13	0.07	0.11	
ZrO ₂	0.00	0.01	Al		0.24		
Ti ₂ O ₃	0.00	0.01	Cr	99.9	99.31	92.1	86.8
Al ₂ O ₃	85.62	21.51	Mn		0.27		
Cr ₂ O ₃	4.74	58.46	total	100.1	99.6	99.9	100.0
V ₂ O ₃	0.01	0.04					
FeO	0.00	0.00					
MnO	0.02	0.14	at. %				
MgO	0.39	18.06	N			18.9	36.1

CaO	0.01	0.18	Si	0.10	0.13		
Na ₂ O	0.07	0.12	Al		0.46		
K ₂ O	9.43	0.00	Cr	99.9	99.15	81.1	63.9
total	100.30	98.53	Mn		0.27		
at. %							
Al	34.40	10.30					
Cr	1.28	18.70					
V							
Mn	0.01	0.10					
Mg	0.02	10.90					
Ca	0.03						
Na	0.10						
K	4.10						
O	60.10	60.00					
Cr#	0.04	0.65					

1175A						
	β-alumina	corundum		spinel	Cr-spin	CrN?
		"core"	"rim"			
wt%	n=4	n=3	n=4	n=5	SEM	SEM
					n=1	n=3
SiO ₂	0.02	0.03	0.01	0.02		N=17
ZrO ₂	0.00	0.02	0.00	0.02		
Ti ₂ O ₃	0.01	0.00	0.00	0.03		
Al ₂ O ₃	74.89	99.18	92.80	48.95	3.44	
Cr ₂ O ₃	9.83	0.73	8.23	26.51	76.4	Cr=83
V ₂ O ₃	0.00	0.01	0.00	0.03		
FeO	0.02	0.00	0.01	0.00		
MnO	0.05	0.00	0.01	0.12		
MgO	7.12	0.02	0.01	21.16	20.1	
CaO	0.16	0.01	0.01	0.05		
Na ₂ O	0.40	0.01	0.02	0.02		
K ₂ O	8.41	0.00	0.00	0.08		
total	100.91	100.00	101.09	97.0	99.9	
at.%						
Si	0.01			0.01		
Al	32.11	39.80	37.75	20.91	1.71	
Cr	2.82	0.19	2.25	7.60	25.6	56.8
Mg	3.78			11.43	12.7	
Na	0.35					
K	3.90					
O	56.97	60.0	60.0	60.1	60.1	
N						43.2
Cr#	0.081	0.005	0.06	0.27	0.94	

Table 4. Individual Cr-ruby grains with Cr inclusions

	1210A-1					1210A-2			1210B-1	
	β -alumina	corundum			Cr-alloy	β -alumina	corundum		β -alumina	
		cores	inner rims	outer rims	(metal %)		cores	rims	laths	overgrowths
wt %	n=3	n=3	n=4	n=3	n=2	n=1	n=4	n=7	n=6	n=5
SiO ₂	0.01	0.00	0.01	0.01	0.09	0.15	0.01	0.03	0.01	0.09
ZrO ₂	0.01	0.01	0.00	0.00		0.02	0.00	0.00	0.01	0.00
Ti ₂ O ₃	0.00	0.00	0.00	0.02		0.00	0.00	0.00	0.00	0.00
Al ₂ O ₃	86.32	98.00	77.03	60.26	0.05	79.20	98.51	81.73	89.74	71.17
Cr ₂ O ₃	1.87	2.22	22.64	39.74	99.45	6.63	0.74	16.70	1.83	17.64
V ₂ O ₅	0.01	0.01	0.03	0.03		0.00	0.01	0.01	0.00	0.02
FeO	0.00	0.00	0.00	0.02		0.00	0.01	0.01	0.01	0.01
MnO	0.01	0.00	0.05	0.09	0.32	0.06	0.00	0.03	0.00	0.06
MgO	0.07	0.01	0.02	0.01		1.57	0.01	0.02	0.08	0.78
CaO	0.01	0.00	0.00	0.01		0.06	0.00	0.00	0.01	0.07
Na ₂ O	0.03	0.00	0.00	0.01		0.17	0.00	0.00	0.02	0.04
K ₂ O	12.65	0.00	0.00	0.00		13.09	0.00	0.00	8.05	10.75
total	100.99	100.24	99.78	100.19	99.91	100.96	99.27	98.54	99.78	100.63
at. %										
Ti				0.02						
Al	34.04	39.37	33.36	27.68		31.57	39.79	35.15	35.16	29.78
Cr	0.49	0.6	6.58	12.24		1.77	0.20	4.82	0.52	4.90
V	0.00		0.01	0.01						
Fe										
Mn			0.02	0.03		0.02		0.01		0.02
Mg	0.03		0.01	0.01		0.79	0.01	0.01	0.39	0.41
Ca						0.02				0.02
Na	0.02					0.11			0.02	0.02
K	5.40					5.96			3.86	4.82
O	60.00	60.00	60.00	60.00		59.8	60.00	60.00	60.10	60.00
Cr#	0.00	0.015	0.165	0.307		0.05	0.005	0.121	0.015	0.141

1210B-1 (cont.)			1210B-2					
wt%	corundum		Cr-Fe alloy	corundum			Cr-alloys	
	cores	rims	SEM	cores	rims	outermost	(metal %)	
	n=4	n=6	n=5	n=4	n=4	n=2	n=5	n=1
SiO ₂	0.01	0.00	(metal %)	0.01	0.03	0.01	0.24	0.12
ZrO ₂	0.04	0.00		0.01	0.01	0.01	0.00	0.00

Ti ₂ O ₃	0.00	0.03	0.11	0.02	0.09	0.03	0.00	0.00
Al ₂ O ₃	93.91	64.01	82.5	97.50	85.36	61.66	99.39	88.46
Cr ₂ O ₃	5.96	35.63	16.2	2.99	14.23	36.66	0.00	0.00
V ₂ O ₅	0.01	0.02	1.06	0.00	0.01	0.02	0.00	0.01
FeO	0.02	0.00	99.97	0.00	0.00	0.00	0.00	11.00
MnO	0.00	0.06		0.01	0.02	0.06	0.26	0.00
MgO	0.00	0.01		0.01	0.01	0.01	0.00	0.00
CaO	0.00	0.00		0.00	0.00	0.01	0.00	0.23
Na ₂ O	0.00	0.01		0.00	0.01	0.02	0.00	0.00
K ₂ O	0.00	0.03		0.00	0.01	0.02	0.00	0.00
total	99.96	99.80		100.54	99.76	98.48	99.89	99.82
at.%								
Zr	0.01							
Ti		0.01	0.21		0.03	0.01		
Al	38.1	29.09	83.6	39.16	35.94	28.56	99.50	
Cr	1.51	10.86	15.3	0.81	4.02	11.39	0.19	
V			0.80			0.01		
Fe								
Mn		0.02			0.01	0.02		
Mg								
Ca								
Na								
K								
O	60.4	60.0		60.03	60.00	60.01		
Cr#	0.038	0.272		0.020	0.101	0.285		

	1210B-3			1210B-5			
	β"-alumina	Corundum		Cr alloy	corundum		β"-alumina
wt%		cores	rim	metal %	cores	rims	
	n=4	n=6	n=1	n=1	n=6	n=4	n=6
SiO ₂	0.00	0.01	0.02				
ZrO ₂	0.00	0.01	0.01				
Ti ₂ O ₃	0.00	0.00	0.00			0.02	
Al ₂ O ₃	80.22	99.49	93.36			0.01	
Cr ₂ O ₃	5.38	0.72	6.98	99.6	99.96	94.98	79.05
V ₂ O ₅	0.01	0.00	0.01		0.41	5.64	5.23
FeO	0.00	0.00	0.00		0.02		0.02
MnO	0.00	0.01	0.02	0.31	0.02		0.05
MgO	6.16	0.00	0.02		0.01		7.95
CaO	0.01	0.00	0.00				0.01
Na ₂ O	0.01	0.00	0.00				0.01

K ₂ O total	8.46 100.21	0.00 100.25	0.00 100.41	99.89	100.37	100.81	8.49 100.81
at.%							
Al	31.83	39.73	38.08		39.87	38.45	31.03
Cr	1.43	0.26	1.91		0.11	1.53	1.38
V					0.01	0.01	0.01
Fe					0.01	0.01	0.01
Mn			0.01			0.01	0.01
Mg	3.09		0.01				3.95
Ca							
Na	0.01						0.01
K	3.63						3.61
O	60.01	60.01	59.99		60.00	59.99	59.99
Cr#	0.043	0.007	0.048		0.003	0.038	0.043

Figure 1

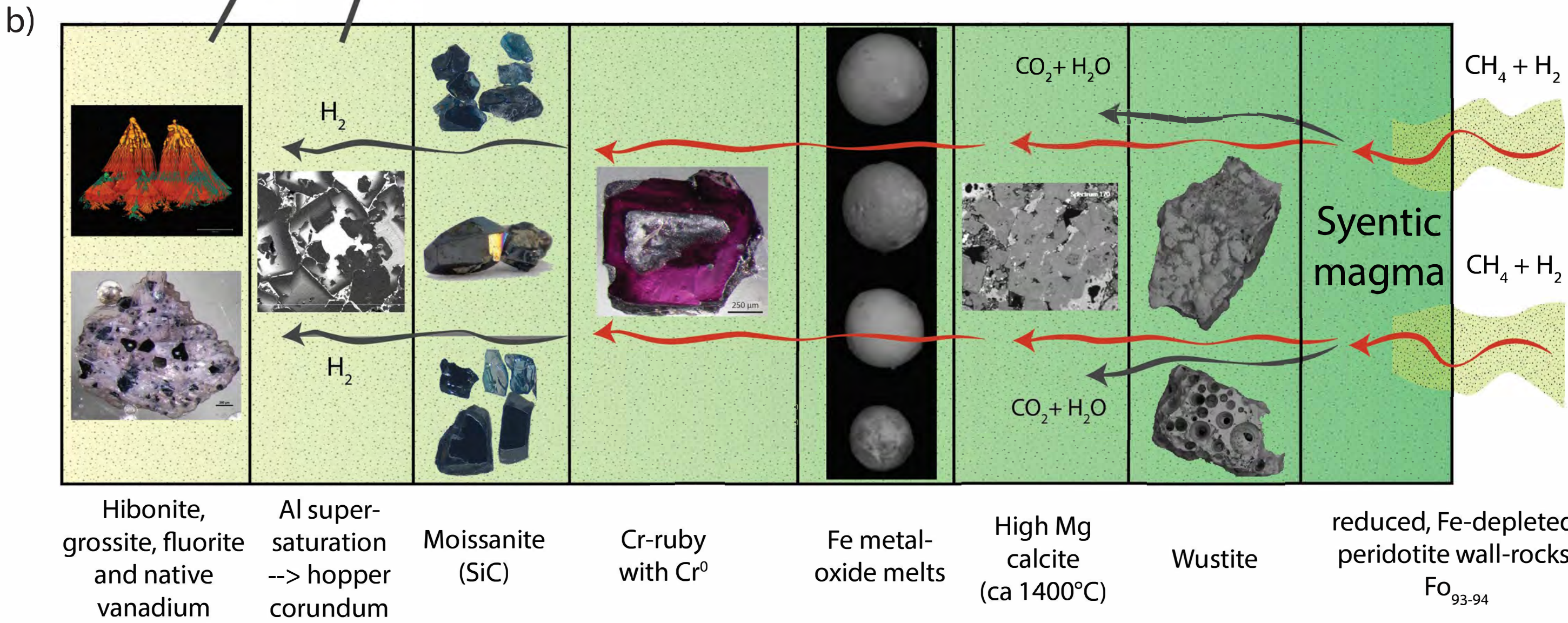
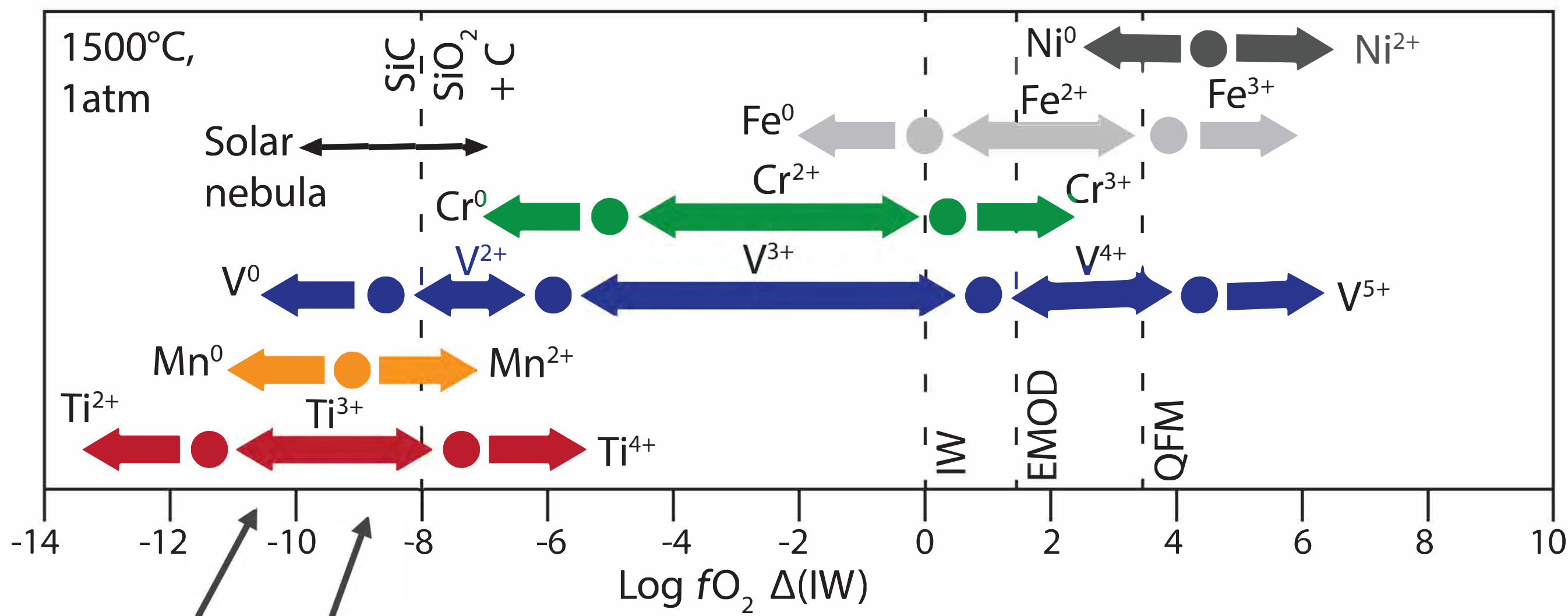


Figure 2

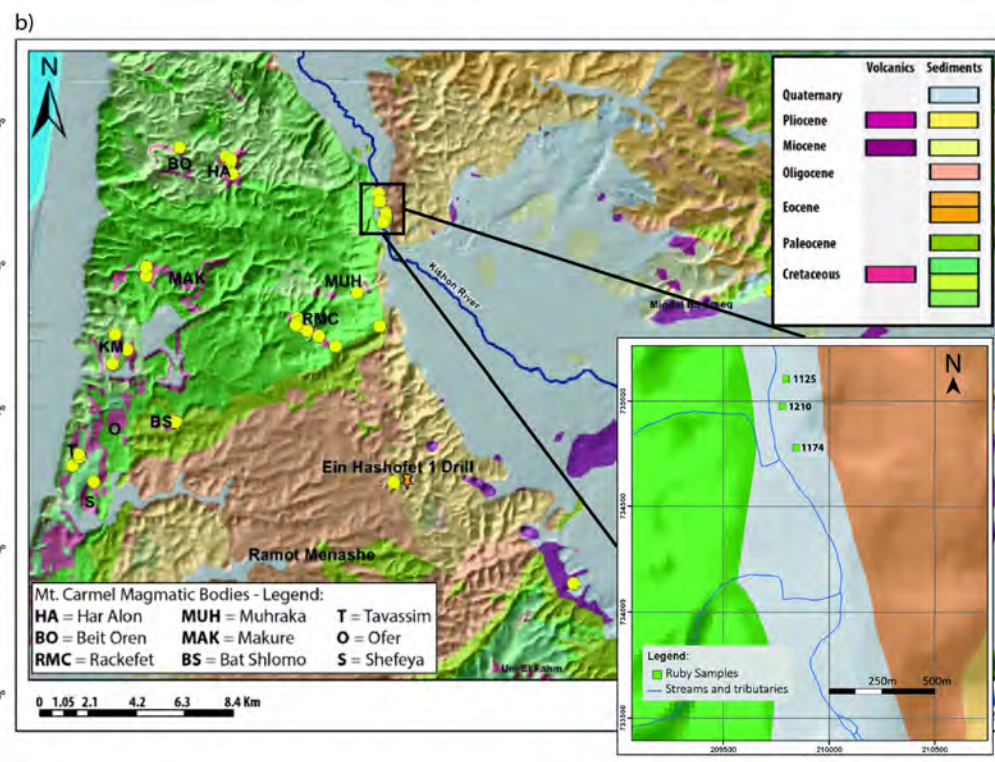
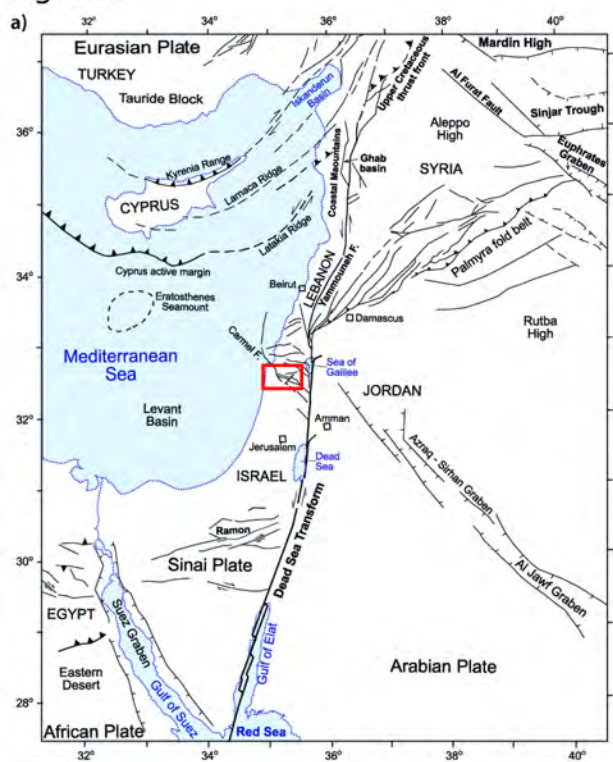


Figure 3



Figure 4

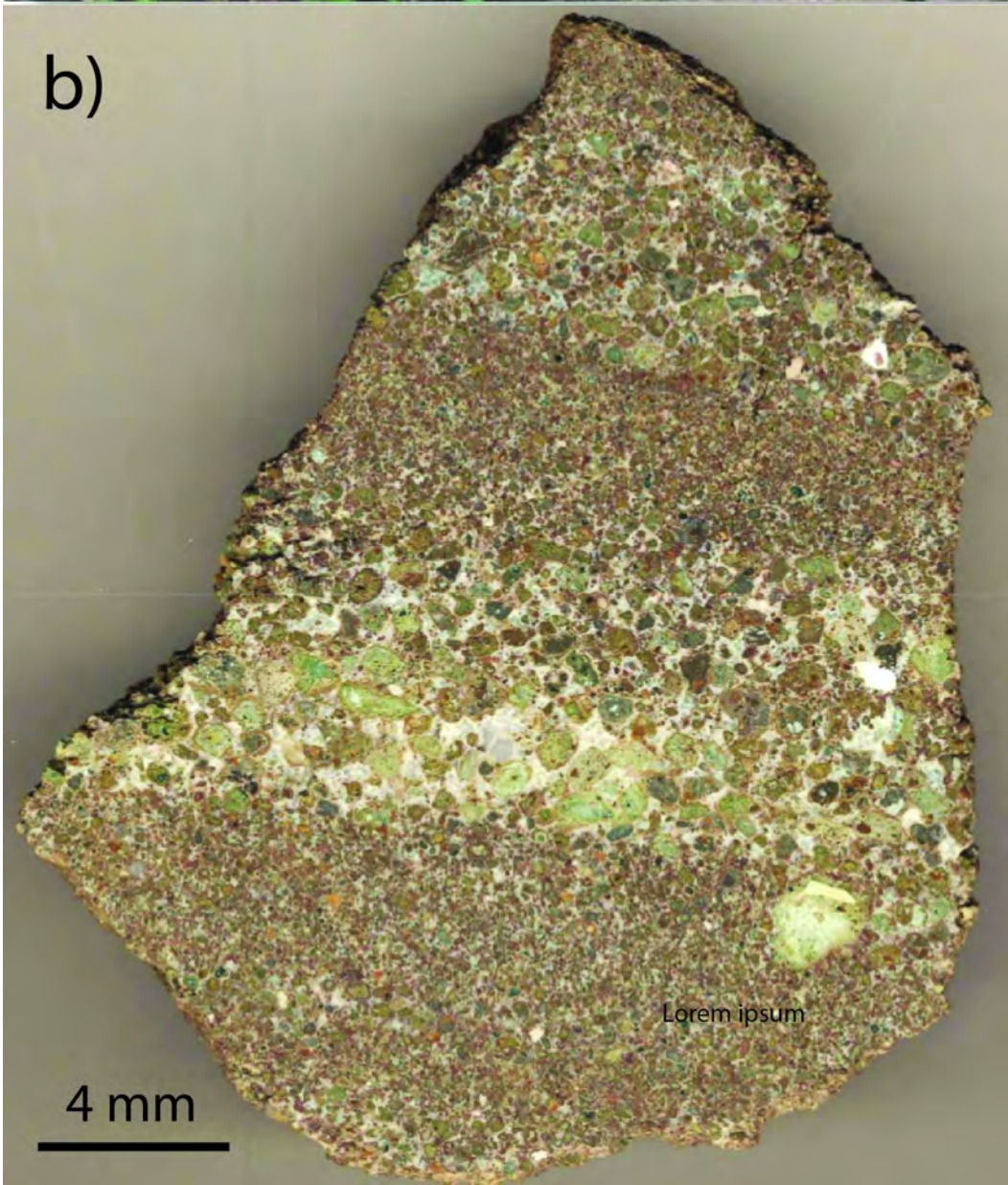


Figure 5

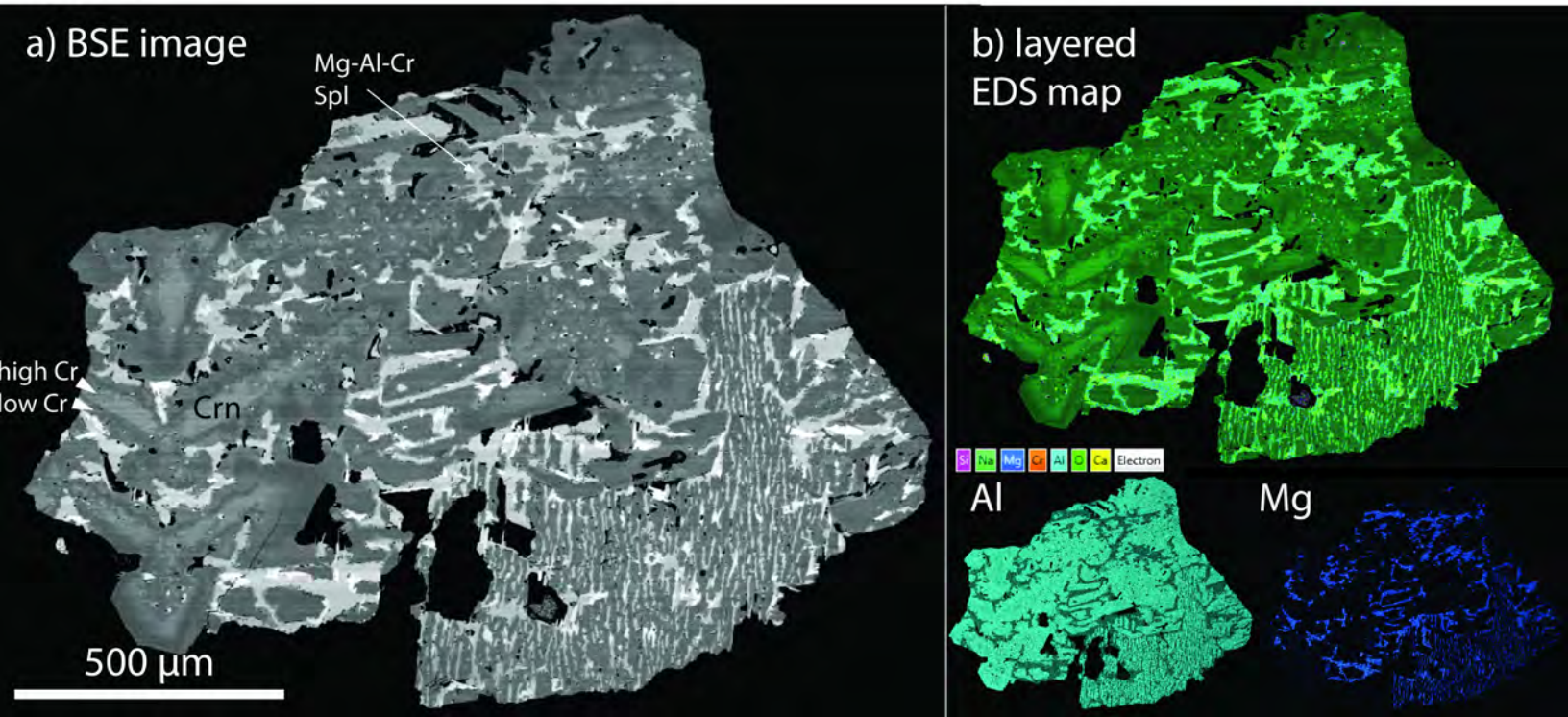


Figure 6

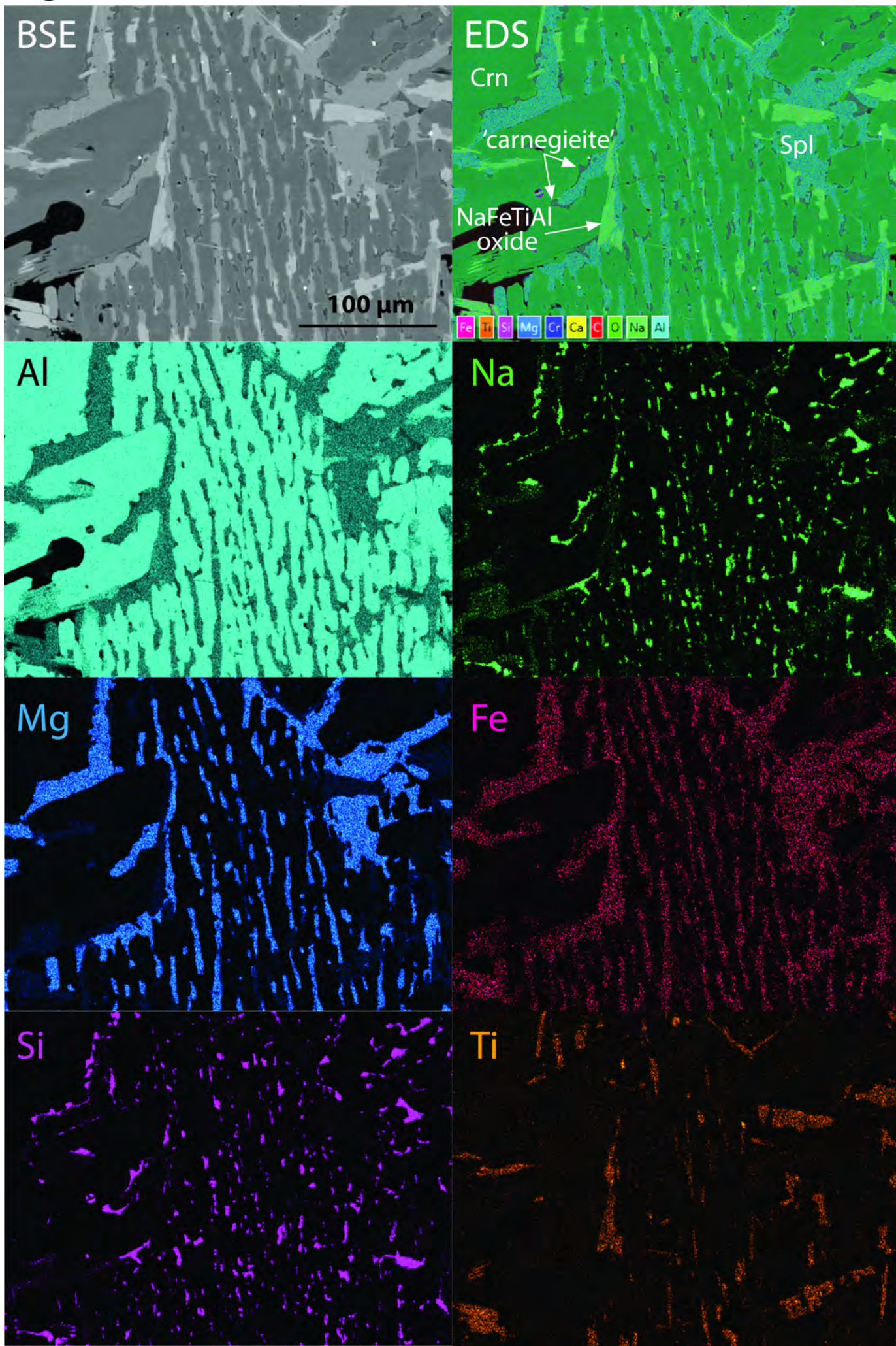


Figure 7

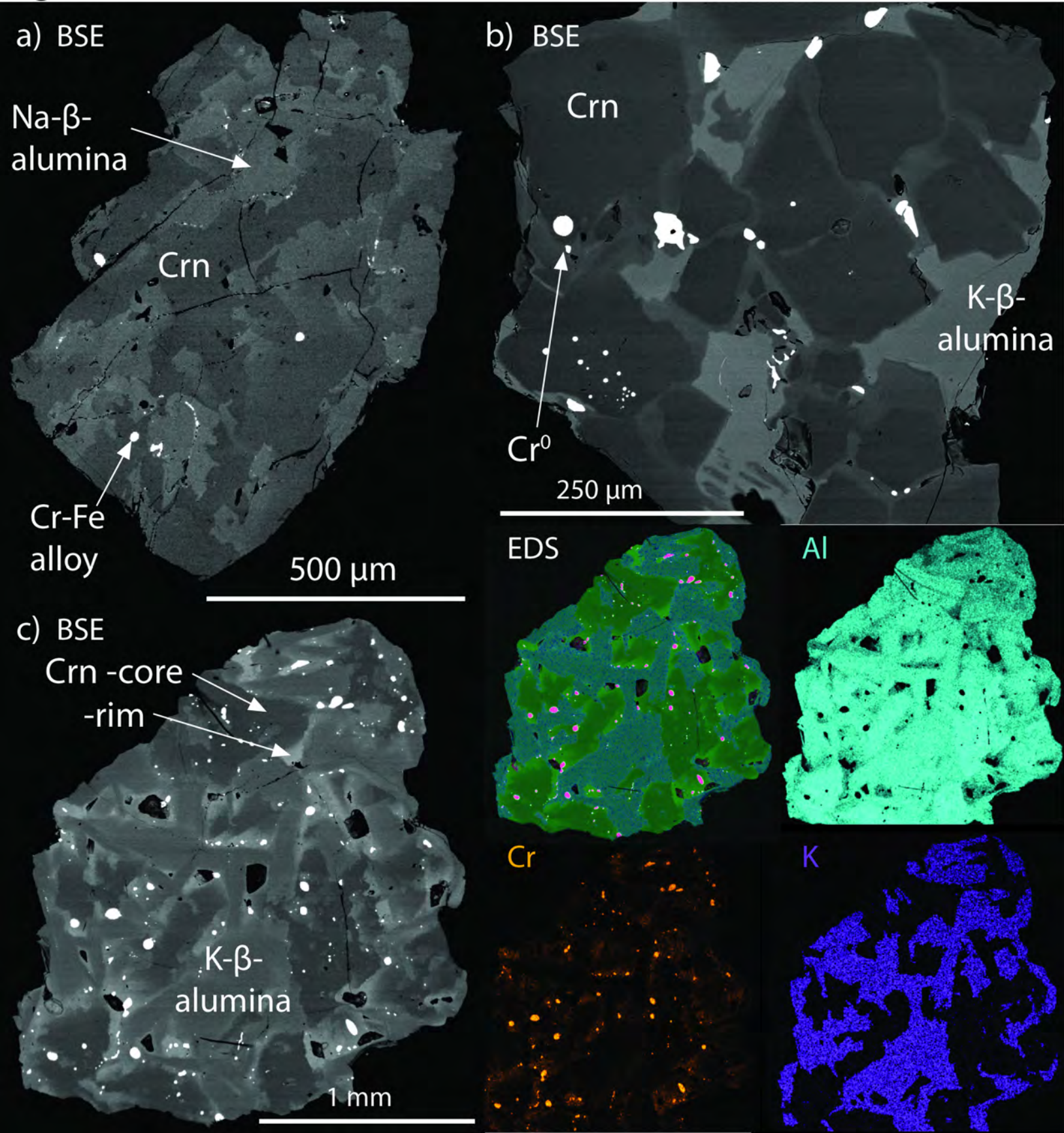


Figure 8

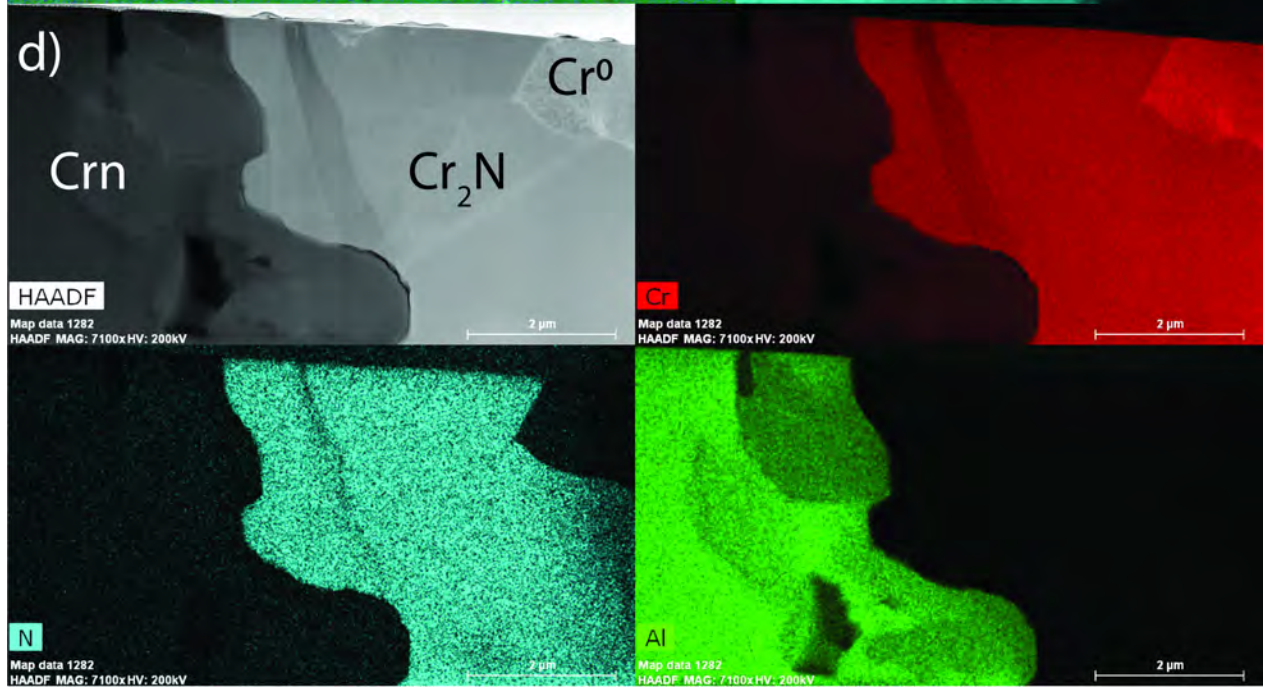
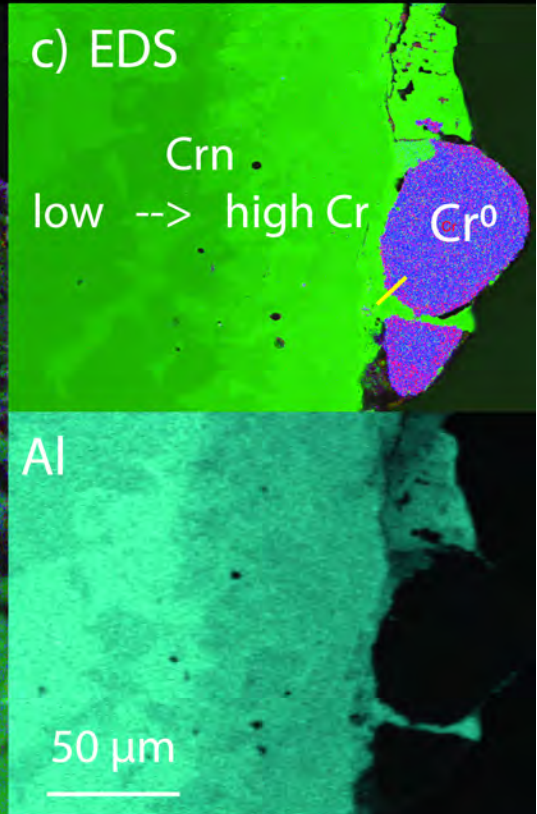
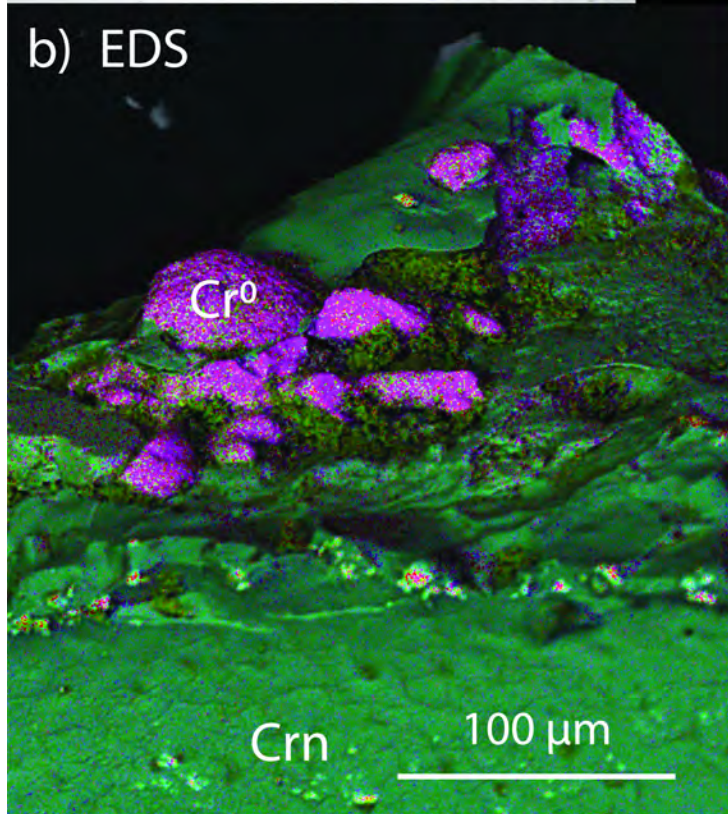
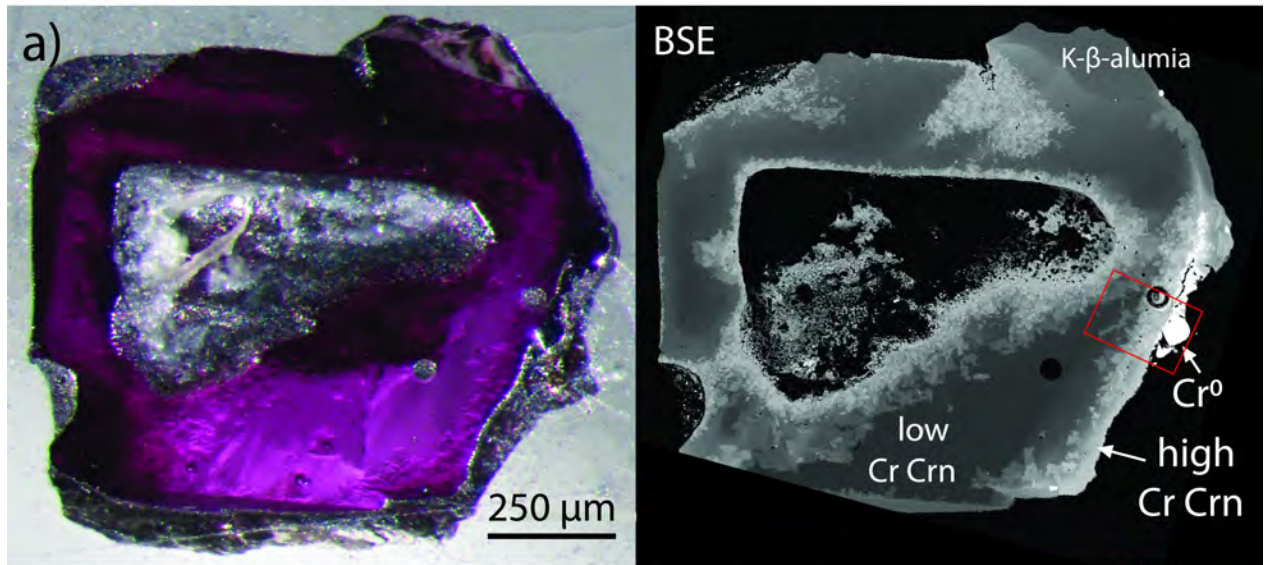


Figure 9

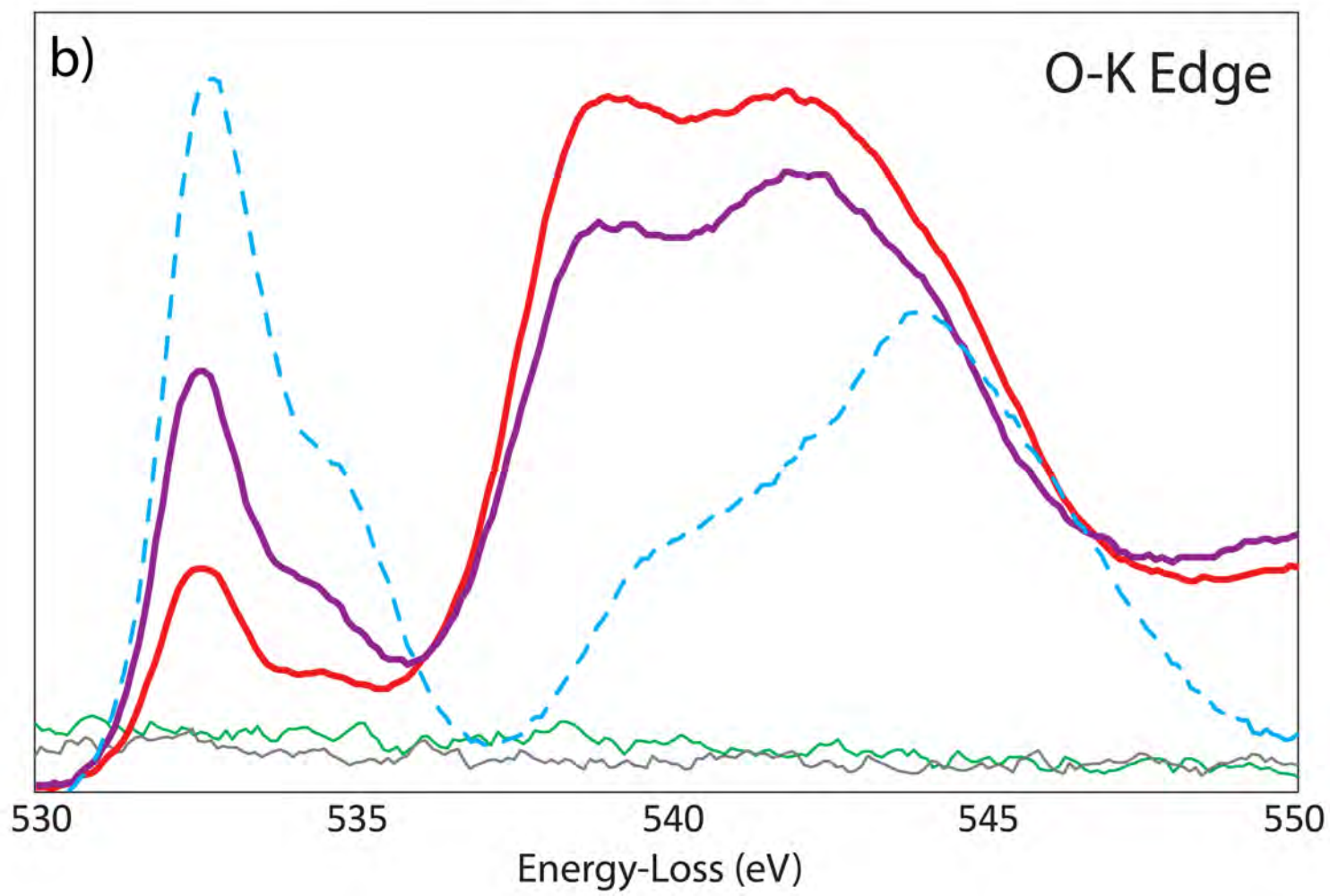
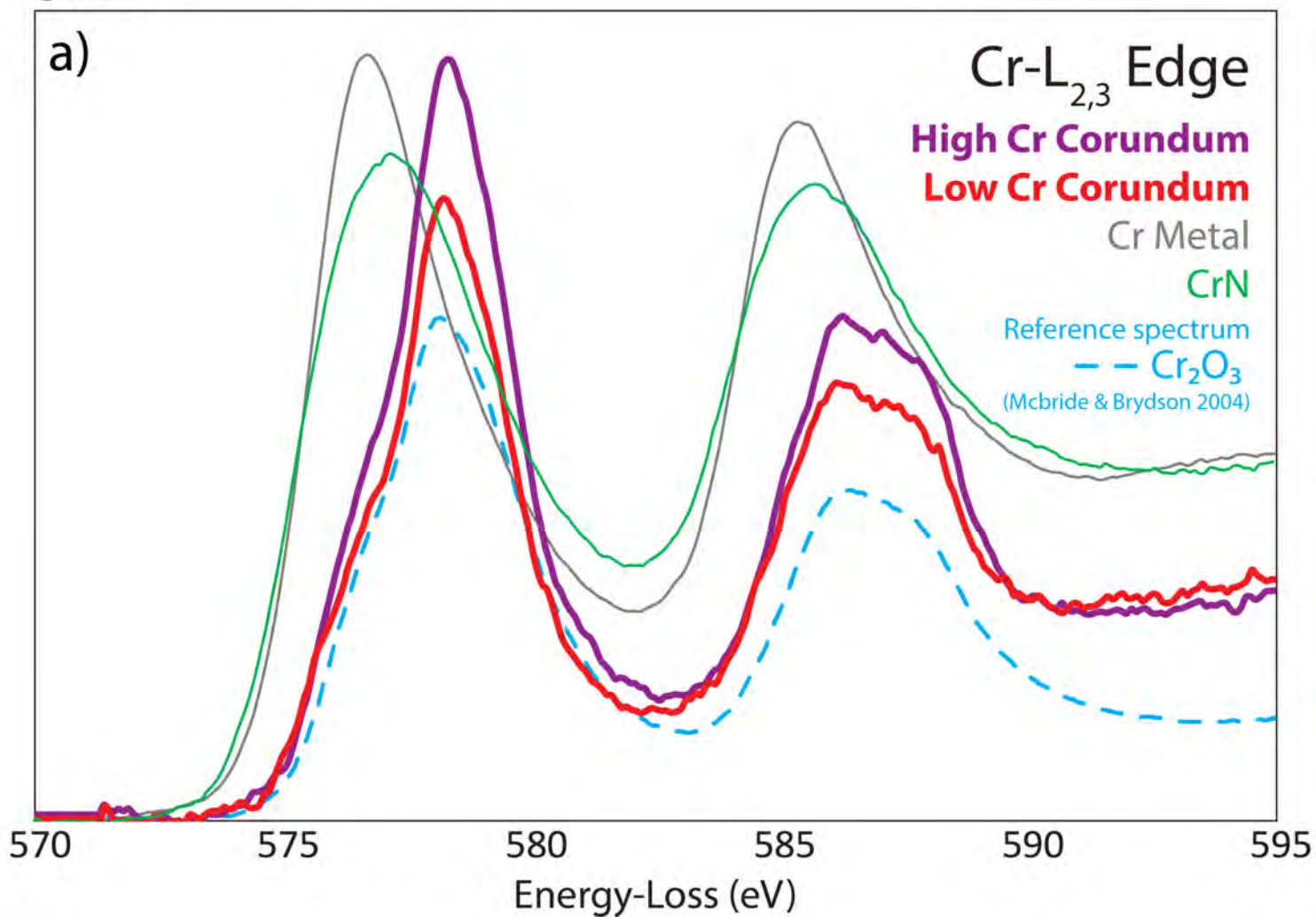


Figure 10

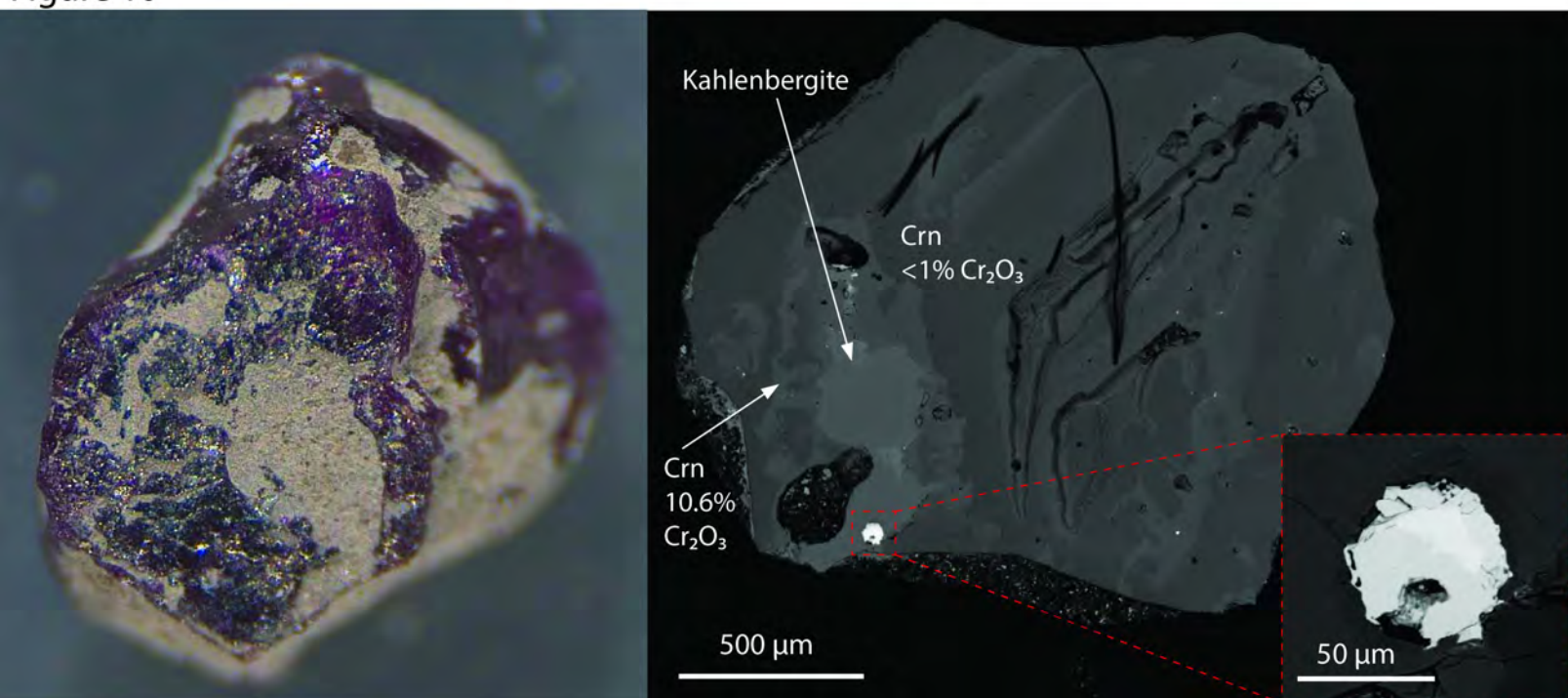


Figure 11

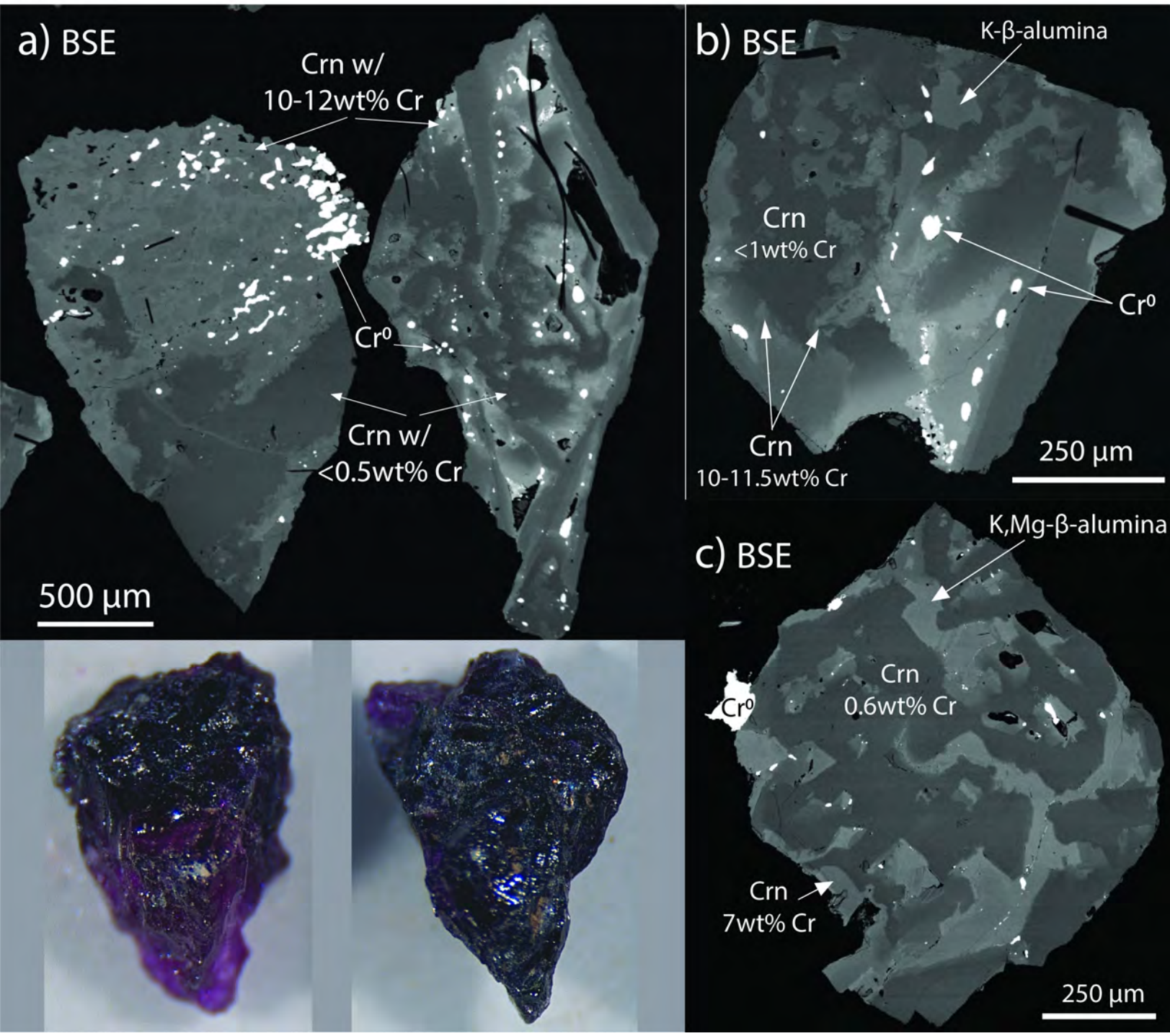


Figure 12

Cr - N

Data from SGTE 2007 alloy database

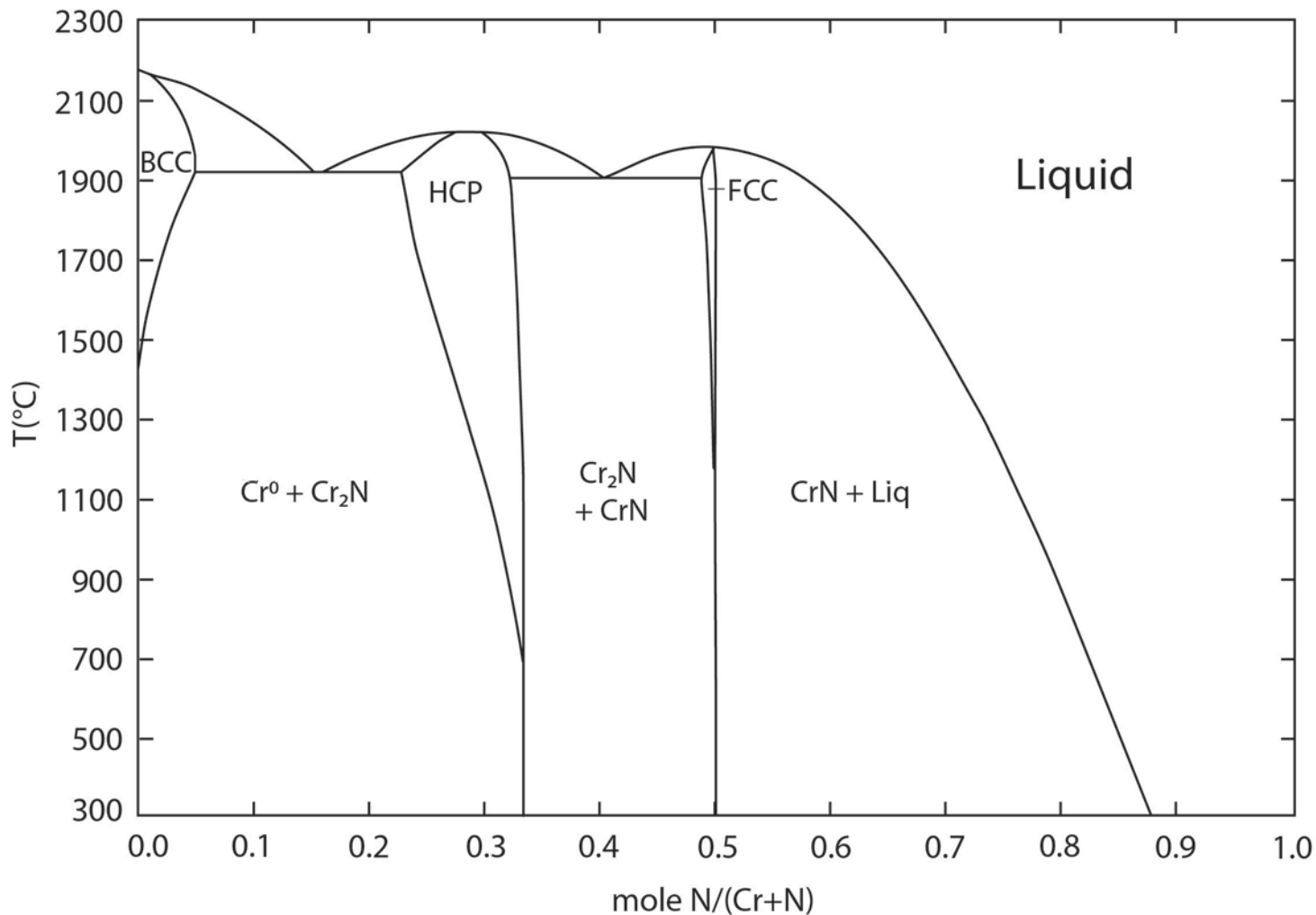


Figure 13

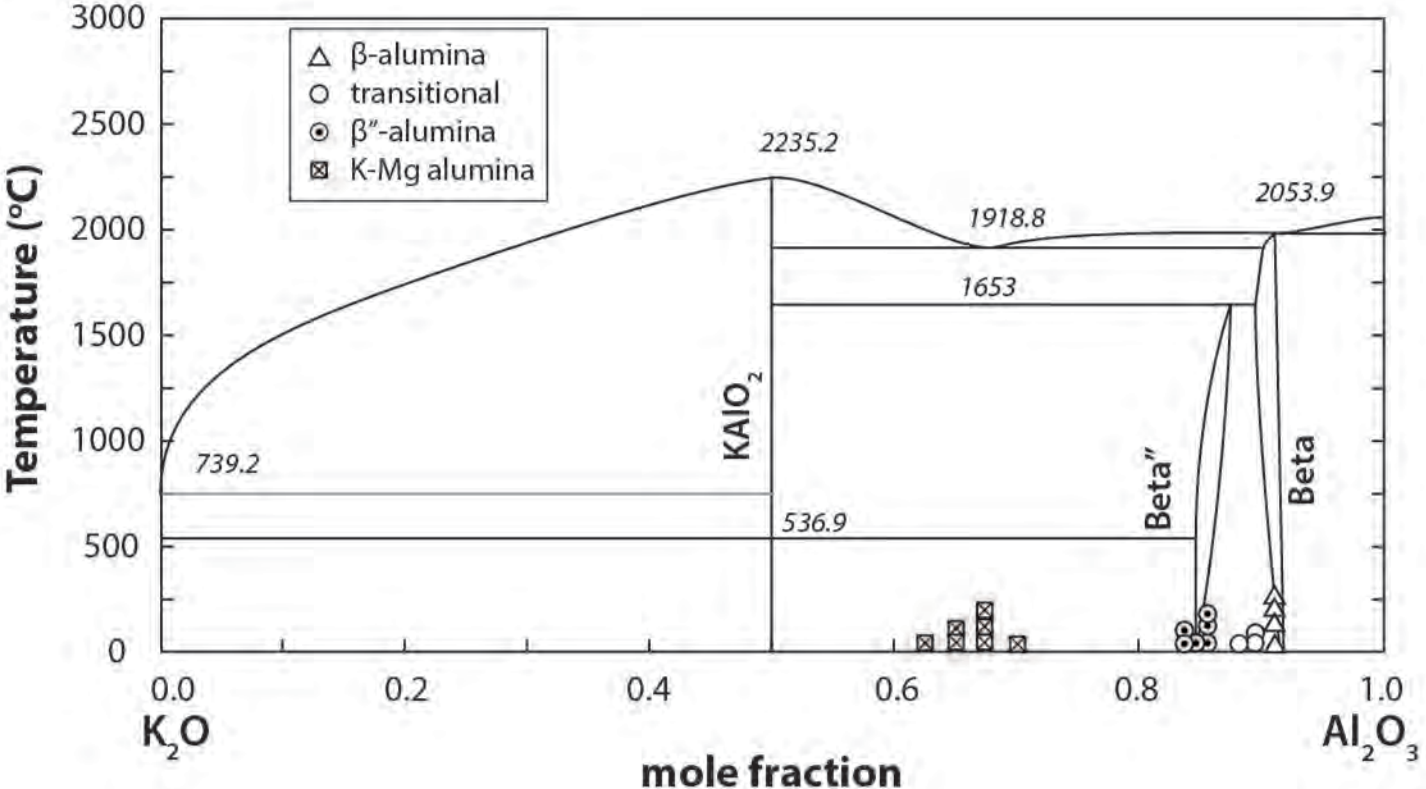


Figure 14

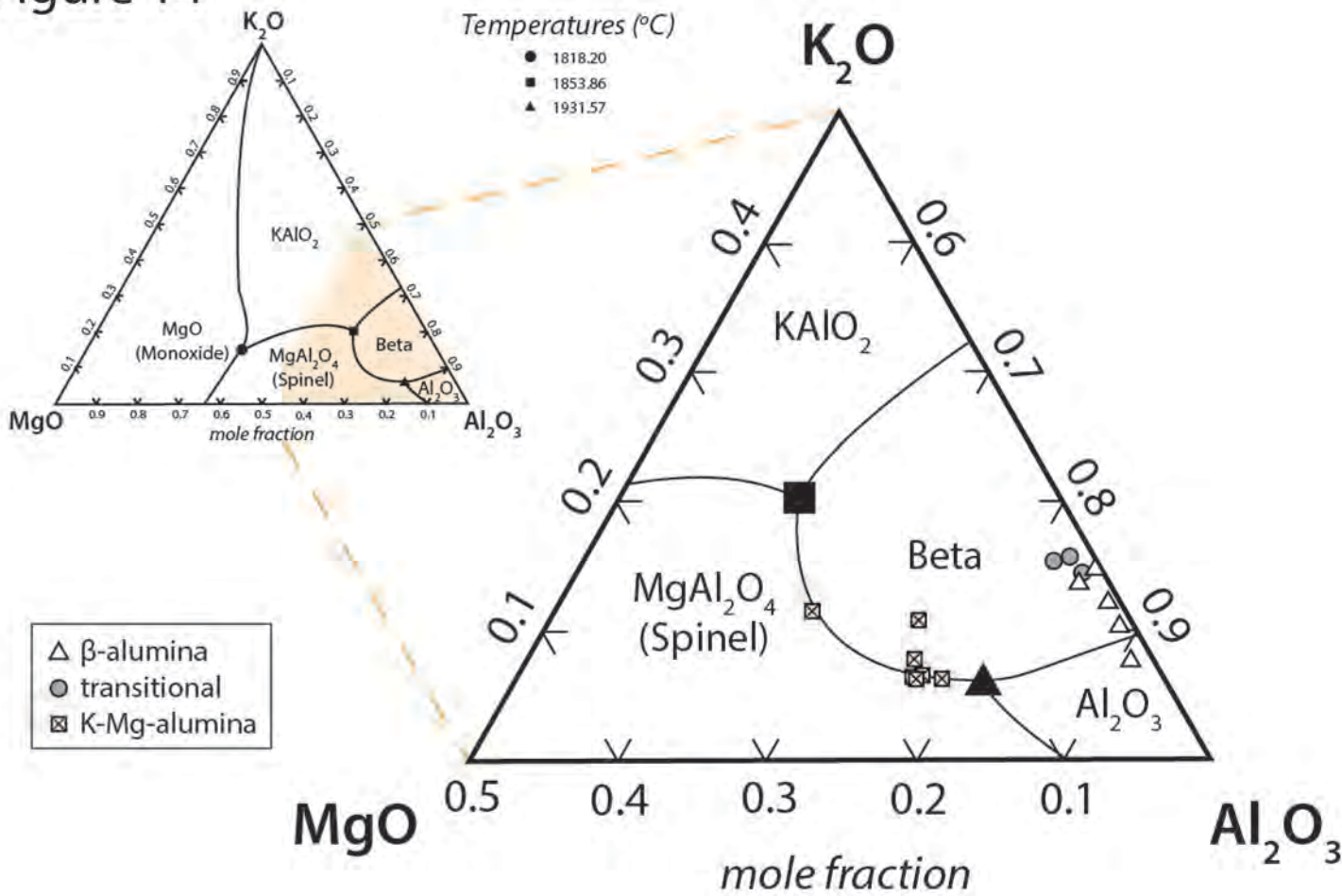


Figure 15

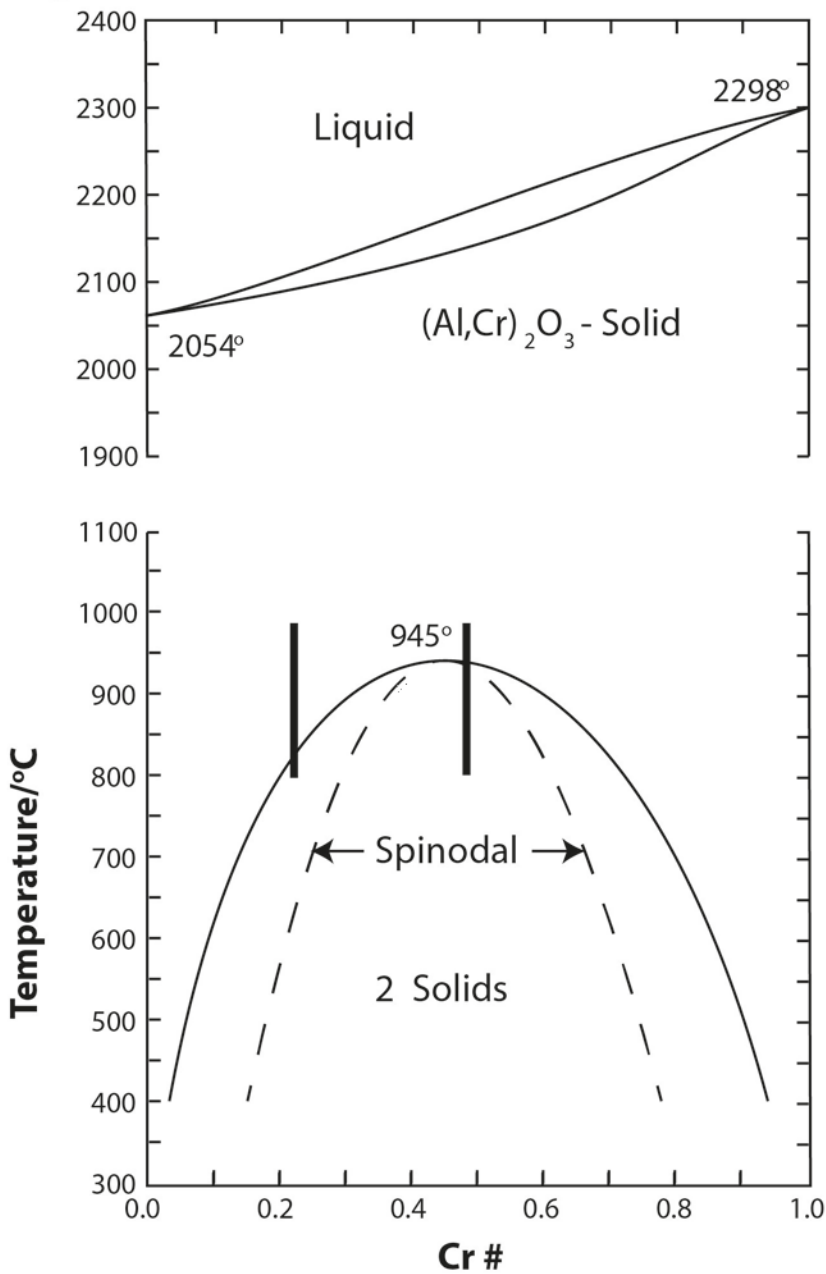


Figure 16

